An Atom-Probe Tomography Study of Phase Separation in Fe-Cr Based Steels

Jing Zhou

Doctoral Thesis

Department of Materials Science and Engineering
KTH Royal Institute of Technology
SE-100 44 Stockholm, Sweden

Stockholm, 2014

Jing Zhou *An Atom-Probe Tomography Study of Phase Separation in Fe-Cr Based Steels*

KTH Royal Institute of Technology,

School of Industrial Engineering and Management,

Department of Materials Science and Engineering,

Division of Physical Metallurgy,

SE-10044, Stockholm

Sweden

ISBN 978-91-7595-195-9

Akademisk avhandling som med tillstånd av Kungliga Tekniska Högskolan i Stockholm, framlägges för offentlig granskning för avläggande av Teknologie doktorsexamen, måndag den 29 september 2014 kl. 10:00 i F3, Lindstedsvägen 26, Kungliga Tekniska Högskolan, Stockholm.

Printed by Universitetsservice US-AB, Stockholm, Sweden

天行健，君子以自强不息；地势坤，君子以厚德载物。

--《周易》

As heaven maintains vigor through movements, a man should constantly strive for self-perfection; As earth's condition is receptive devotion, a man should hold the outer world with broad mind. --≪Zhou Yi≫

To Ruifang

如果一个人没有能力帮助他所爱的人，最好不要随便谈什么爱与不爱。当然，帮助不等于爱情，但爱情不能不包括帮助。 ——鲁迅

Abstract

Stainless steels are very important engineering materials in a variety of applications such as in the food industry and nuclear power plants due to their combination of good mechanical properties and high corrosion resistance. However, ferrite-containing stainless steels are sensitive to the so-called '475°C embrittlement', which is induced by phase separation of the ferrite phase, where it decomposes into Fe-rich ferrite (α) and Cr-rich ferrite (α'). The phase separation is accompanied with a severe loss of toughness. Therefore, the upper service temperature of ferrite-containing stainless steels in industrial applications has been limited to around 250 °.

In the present work, Fe-Cr based steels were mainly investigated by atom probe tomography. A new method based on the radial distribution function (RDF) was proposed to quantitatively evaluate both the wavelength and amplitude of phase separation in Fe-Cr alloys from the atom probe tomography data. Moreover, a simplified equation was derived to calculate the amplitude of phase separation. The wavelength and amplitude was compared with evaluations using the auto-correlation function (ACF) and Langer-Bar-on-Miller (LBM) method, respectively. The results show that the commonly used LBM method underestimates the amplitude of phase separation and the wavelengths obtained by RDF shows a good exponential relation with aging time which is expected from the theory. The RDF is also an effective method in detecting the phenomena of clustering and elemental partitioning.

Furthermore, atom probe tomography and the developed quantitative analysis method have been applied to investigate the influence of different factors on the phase separation in Fe-Cr based alloys by the help of mainly mechanical property tests and atom probe tomography analysis. The study shows that: (1) the external tensile stress during aging enhances the phase separation in ferrite. (2) Phase separation in weld bead metals decomposes more rapidly than both the heat-affected-zone metals and the base metals mainly due to the high density of dislocations in the welding bead metals which could facilitate the diffusion. (3) The results show that Ni and Mn can enhance the phase separation comparing to the binary Fe-Cr alloy whereas Cu forms clusters during aging. (4) Initial clustering of Cr atoms was found after homogenization. Two factors, namely, clustering of Cr above the miscibility gap and clustering during quenching was suggested as the two responsible mechanisms. (5) The homogenization temperatures significantly influence the evolution of phase separation in Fe-46.5at.%Cr.

Keywords: Fe-Cr alloys; Ferritic stainless steels; Spinodal decomposition; Phase separation; Atom probe tomography; Radial distribution function (RDF).

Preface

The present doctoral thesis, based partly on my previous licentiate thesis, summarizes the knowledge that I acquired during my 4-years of study as a Ph. D student in the Department of Materials Science and Engineering at KTH Royal Institute of Technology. This work has mainly been part of the Spinodal project within the Hero-m Center, and was supported by Erasmus Mundus Tandem, the Swedish Research Council and the VINNEX center Hero-m which is financed by the Swedish Governmental Agency for Innovation Systems VINNOVA, Swedish Industry and KTH Royal Institute of Technology. Several partners have been directly involved in the project, including Sandvik Materials Technology, Outokumpu Stainless, Outokumpu Stainless Research Foundation, Swerea KIMAB and Chalmers University of Technology.

Several challenges are thoroughly discussed in the present thesis:

- ✓ Quantitative and accurate evaluation of the amplitude and wavelength during phase separation in Fe-Cr based alloys.
- ✓ The influence of different factors on the phase separation, such as external stress, defects, alloying elements and solution treatment temperature.

The structure of the thesis is as follows: in Chapter 1, stainless steels are introduced, together with the scope of the present work; in Chapter 2, the physical background of phase separation is explained based on the understanding of thermodynamics; in Chapter 3-4, details regarding the major techniques are given, which presents a brief review of the development on atom probe tomography, its application on phase separation in Fe-Cr alloys and connections between the phase separation and mechanical properties; in Chapter 5, details regarding the methodology are presented; Chapter 6 summarizes the appended papers and Chapter 7 presents the concluding remarks and future work.

Jing Zhou

Stockholm, 2014-08-12

Appended papers

I. Quantitative evaluation of spinodal decomposition in Fe-Cr by atom probe tomography and radial distribution function analysis
Jing Zhou, Joakim Odqvist, Mattias Thuvander and Peter Hedström.
Microscopy and Microanalysis, Volume 19, 665-675, 2013.

II. Observations of Cu clustering in a 25Cr-7Ni super duplex stainless steel during low temperature aging under load
Mattias Thuvander, Jing Zhou, Joakim Odqvist, Staffan Hertzman and Peter Hedström.
Philosophical Magazine Letters, Volume 92, Issue 7, 336-343, 2012.

III. Concurrent phase separation and clustering in the ferrite phase during low temperature stress-aging of duplex stainless steels
Jing Zhou, Joakim Odqvist, Mattias Thuvander, Staffan Hertzman and Peter Hedström.
Acta Materialia, Volume 60, 5818-5827, 2012.

IV. Initial clustering - a key factor for phase separation kinetics in Fe-Cr based alloys
Jing Zhou, Joakim Odqvist, Peter Hedström, Lars Höglund, Mattias Thuvander, Thomas Barkar and Peter Hedström.
Scripta Materiallia, Volume 75, 62-65, 2014.

V. The 475 °C embrittlement in Fe–20Cr and Fe–20Cr–X (X=Ni, Cu, Mn) alloys studied by mechanical testing and atom probe tomography
Peter Hedström, Fei Huyan, Jing Zhou, Sten Wessman, Mattias Thuvander and Joakim Odqvist.
Materials Science and Engineering A, Volume 574, 123-129, 2013.

VI. Direct atom probe tomography observations of concentration fluctuations in Fe-Cr solid solution
Jing Zhou, Joakim Odqvist, John Ågren, Andrei Ruban, Mattias Thuvander, Wei Xiong, Gregory B. Olson and Peter Hedström.
In manuscript.

VII. Effect of homogenization temperature on subsequent spinodal decomposition during aging in Fe-46.5Cr alloy
Jing Zhou, Joakim Odqvist, Mattias Thuvander, Wei Xiong, John Ågren, Gregory B. Olson and Peter Hedström.
In manuscript.

The author's contribution to the papers listed above:

Paper I: Major part of literature survey, experimental work, data analysis and manuscript.

Paper II: Major part of experimental work, contributed to discussion and manuscript.

Paper III: Major part of literature survey, experimental work, data analysis and manuscript.

Paper IV: Major part of literature survey, experimental work, data analysis and manuscript.

Paper V: Major part of atom probe analysis, contributed to discussion and manuscript.

Paper VI: Large part of literature survey, experimental work, data analysis and manuscript.

Paper VII: Major part of literature survey, experimental work, data analysis and manuscript.

Contents

Chapter 1

Introduction

1.1 Stainless steels

Stainless steels have an attractive combination of good corrosion resistance and excellent mechanical properties and are widely used in modern society, e.g. as tubes in nuclear power plants and chemical industry and cans in the food industry. Although stainless steels have been studied for more than a century, they are still developed further for improved performance in even harsher environments.

In general, stainless steels are mainly composed of Fe and Cr, with some other alloying elements as well to meet the specific practical needs. For instance, Mo is added to enhance the resistance against pitting corrosion and Ni is an austenite-stabilizing element, which is added to enable a duplex microstructure with both ferrite and austenite to combine the merits of both phases. As a rule of thumb, the steel must contain more than 10.5 wt. % Cr (Bernstein, 1977) in order to achieve the aim of being stainless. The corrosion resistance stems from a dense layer of chromium oxide that forms on the steel surface and protects the underlying steel from further corrosion when exposed to a corrosive environment.

In principle, stainless steels can be categorized into four groups depending on their different microstructures: ferritic, austenitic, martensitic and duplex stainless steels. The formation of different microstructures is highly dependent on the alloying elements added and heat treatments. In addition to the microstructures mentioned above, other phases and precipitates may form at different temperatures and alloy compositions, e.g. σ phase (Hall & Algie, 1966), χ phase (Kasper, 1954), π phase (Nilsson & Liu, 1991) and G phase (Vitek, 1987). However, the biggest challenge for the application of ferrite-containing stainless steels at intermediate or even lower temperatures is the formation of α' in ferrite which induces a significant decrease of ductility. This phenomenon has been named ‘475°C Embrittlement’ since the formation of α' is detrimental to the material’s mechanical properties, and is fastest when aging around 475°C (Fisher et al., 1953). The physical background for the precipitate of α' is the existence of a miscibility gap in the Fe-Cr binary phase diagram, as shown in Fig. 1.1. As a consequence of the existing miscibility gap, the ferrite decomposes into Fe-rich phase (α) and Cr-rich phase (α'). The strain induced between α and α' could increase the hardness and decrease the ductility. Therefore, in order to overcome or suppress this phenomenon, extensive effort is needed to understand the mechanisms and the influence of different factors, for instance, heat treatment and alloying composition.

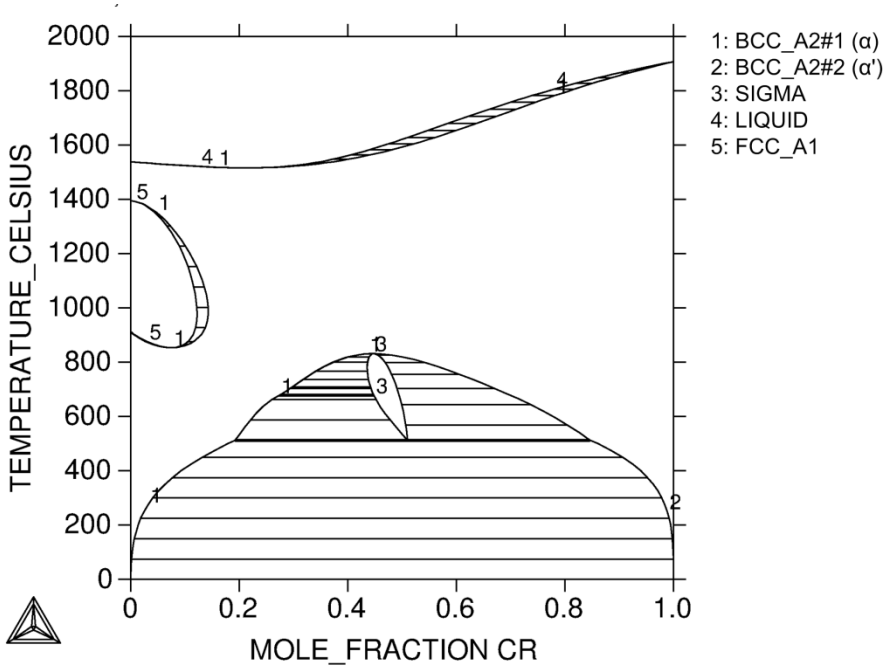

Figure 1.1 Phase diagram of binary Fe-Cr calculated with Thermo-Calc using the TCFE6 database (Thermo-Calc, 2008).

1.2 Scope of the present work

The present thesis is directed towards an experimental investigation of phase separation in Fe-Cr based ferrite-containing stainless steels.

One of the challenges in this work has been to quantitatively evaluate the wavelength and amplitude of the phase separation in Fe-Cr alloys based on the data obtained from atom probe tomography. Although several methods have been proposed for this purpose, there are several disadvantages with these methods. One main contribution of the present work has been the development of a new method based on the radial distribution function to quantitatively evaluate the wavelength and amplitude of the phase separation in Fe-Cr alloys. The results from the new method have been compared with results from other methods as well, such as the auto-correlation function for determining the wavelength (Brenner et al., 1984) and the Langer-Bar-on-Miller (LBM) method (Langer et al., 1975) and the variation method (Blavette et al., 1988) for determining the amplitude. In addition, a simple and easily-used equation has been derived to evaluate the amplitude. Furthermore, the radial distribution function shows its great efficiency in detecting clustering and elemental partitioning.

Another challenge has been to investigate the influence of different factors on phase separation in Fe-Cr based ferritic alloys. In order to find an effective way to suppress the '475°C Embrittlement', several factors have been investigated, including the initial structure, external stress, defects, alloying elements and solution temperatures. The main experimental technique has been atom probe tomography, which has been complemented with mechanical

properties tests including hardness measurements and impact toughness testing, and structural characterization by TEM, SEM and EBSD. The influence of initial structure on phase separation in Fe-Cr alloys was investigated by both experiments and phase-field modeling. The effect of defects on the evolution of phase separation was discussed. Three alloying elements, e.g. Ni, Mn and Cu were investigated regarding their influence on the embrittlement and hardening compared to the binary alloy. The effect of the solution treatment temperature has also been studied by atom probe tomography and hardness tests.

Chapter 2

Phase Separation

2.1 Theory of phase separation

The phase separation in ferritic stainless steels is a type of phase transformation in which there is only a change in composition but not in the crystal structure. Besides in Fe-Cr alloys, phase separation has also been studied in systems such as e.g. Al-Ag (Baur & Gerold, 1962), Al-Zn (Larsson, 1967), Au-Ni (Woodilla & Averbach, 1968), Au-Pt (Meijering, 1961) and (Ti, Zr)C (Holleck, 1986; Borgh et al., 2014). The theory of phase separation originates from a doctoral thesis by Hillert in the 1950s (Hillert, 1956). Later, the theory was extended and developed further by Cahn and Hilliard (Cahn & Hilliard, 1958) and Cahn (Cahn, 1961). Langer et al. (Langer et al., 1975) proposed a new modeling method taking into account fluctuations and the non-linearity of the thermodynamic factor.

The mechanism of phase separation is either spinodal decomposition or nucleation and growth. The difference between these two mechanisms can easily be seen in Fig. 2.1(a) and (b). Fig. 2.1(a) shows the mechanism of spinodal decomposition, which is an up-hill diffusion process due to the negative diffusivity inside the spinodal line according to Fig. 2.2(b). Phase separation via the spinodal mechanism is spontaneous and occurs without any incubation time. Between the miscibility gap boundary and the spinodal line in Fig. 2.2(a), the phase separation occurs via nucleation and growth which is a down-hill diffusion process, as shown in Fig. 2.1(b). In this region, the structure is metastable according to the Gibbs energy curve in Fig. 2.2(b). Usually, an incubation time is accompanied with the mechanism of nucleation and growth when aging at intermediate temperatures.

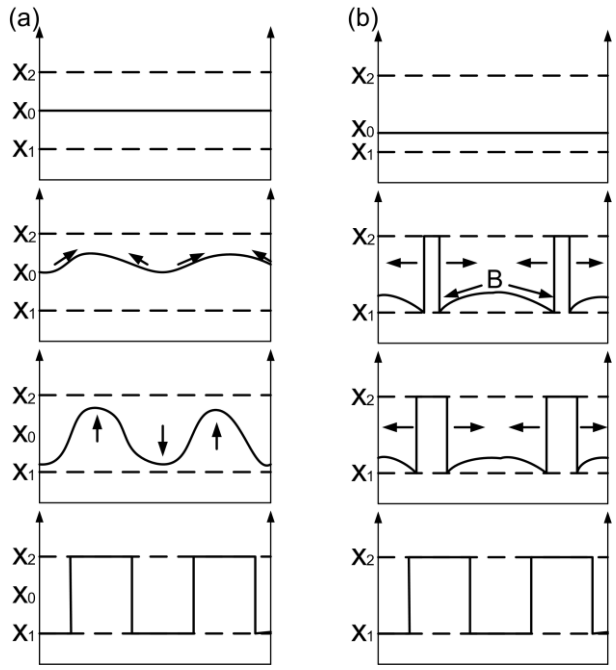

Figure 2.1 Evolution of the two mechanisms of phase separation: (a) spinodal decomposition; (b) nucleation and growth (Porter & Easterling, 1991).

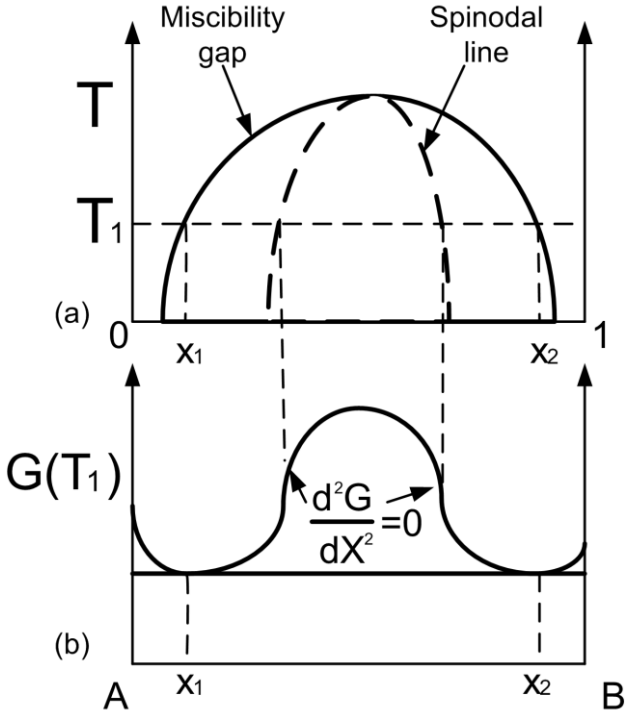

Figure 2.2 (a) Chemical spinodal line and miscibility gap; (b) Gibbs energy at the temperature of T_2 in binary system (Porter & Easterling, 1991).

As can be seen in Fig. 2.3, there exist two kinds of spinodal lines: the chemical spinodal and the coherent spinodal. The difference is that for the chemical spinodal, the interfacial energy and coherency stresses are not considered, but considered in the coherent spinodal.

For the chemical spinodal, a general mathematical treatment of spinodal decomposition is based on the stability limit in a mixture of two different elements, which can be described by Eq. (2.1). This equation determines the boundary of the chemical spinodal where the sign for the curvature of the Gibbs energy changes. Inside the spinodal, the curvature of the Gibbs energy curve is negative and phase separation occurs with a steady decrease in the Gibbs energy.

$$\frac{d^2 G_m}{dX_B{}^2} = 0 \tag{2.1}$$

where G_m is the molar Gibbs energy; X_B is the mole fraction of element B.

In order to model the phase separation in reality, two more parts should be taken into consideration, i.e. the gradient and the strain energy. The gradient energy is caused by the phase-interface between A-rich phase and B-rich phase, i.e. the composition gradient and the strain energy comes from the mismatch between the lattices of the two new phases due to the difference in lattice parameters caused by the composition difference. Thus, the changes of the molar Gibbs energy of the system due to composition gradient can be expressed as Eq. (2.2). In this equation, the second term on the right side of the equation stands for the gradient energy and the third term for the strain energy.

$$\Delta G = \left(\frac{d^2 G_m}{dX_B{}^2} + \frac{2K}{\lambda^2} + 2\eta^2 E' V_m\right) \frac{(\Delta X_B)^2}{2} \tag{2.2}$$

Where λ is the wavelength of the nano-scale spinodal structures; K is a proportionality constant dependent on the difference in the bond energies of like and unlike atom pairs; η is the fractional change in lattice parameter per unit composition change; $E' = E/(1-\nu)$, E is Young's modulus, ν is Poisson's ratio; V_m is the molar volume.

According to Fig. 2.2(b), spinodal decomposition can only occur inside the miscibility line where the second derivative of the Gibbs energy is negative. Thus, Eq. (2.3) can be derived as the condition of spinodal decomposition from the combination of Eqs. (2.1) and (2.2).

$$\frac{d^2 G_m}{dX_B{}^2} + \frac{2K}{\lambda^2} + 2\eta^2 E' V_m < 0 \tag{2.3}$$

It can be seen that the strain energy is always positive and this term thus decreases part of the driving force for spinodal decomposition. The strain-energy term can thus decrease the critical temperature for spinodal decomposition and the temperature drop depends on η. The boundary of the spinodal decomposition is found when $\lambda = \infty$, i.e. Eq. (2.4) gives.

$$\frac{d^2 G_m}{dX_B{}^2} = -2\eta^2 E' V_m \tag{2.4}$$

From Eq. (2.4), it is obvious that the existence of stress between α and α' suppresses both the spinodal and the miscibility gap to lower temperature, as shown in Fig. 2.3. Since the interface between α and α' is coherent and being considered, they are named coherent miscibility gap and coherent spinodal respectively when considering the strain energy.

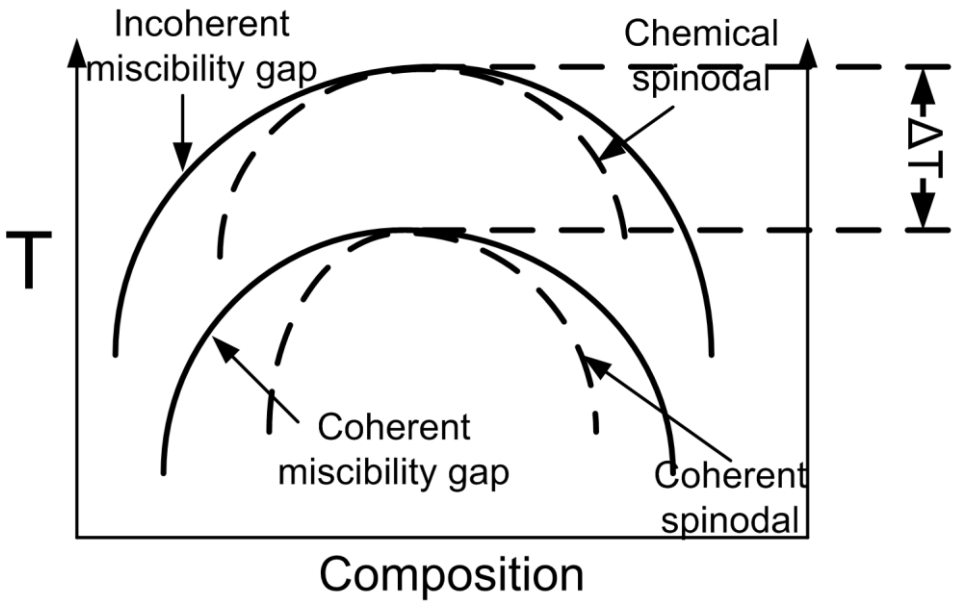

Figure 2.3 Different types of spinodal lines and miscibility gaps (Porter & Easterling, 1991).

Furthermore, the suppression of the critical temperature (ΔT in Fig. 2.3) due to the strain energy can be evaluated by Eq. 2.5 according to Cahn (Cahn, 1961). According to the equation below, given by Cahn, the effect of η on the critical temperature may be calculated. The results are listed in Table 2.1 for different binary systems. Since the radius difference in Fe and Cr is quite small (less than 1%), it has been claimed by that the strain energy has negligible influence on the critical temperature in the binary of Fe-Cr. The result from Eq. (2.5) shows the difference between the chemical and coherent miscibility gaps is no more than 5 ℃.

$$\Delta T = \frac{4\eta^2 E'}{kNv} \tag{2.5}$$

Table 2.1 Critical temperature changes in different binary systems (Cahn, 1961)

Systems	η	ΔT(℃)
Fe-Cr	0.005	4.5
Al-Zn	0.0257	40
Au-Pt	0.038	200
Au-Ni	0.15	2000

2.2 Phase separation in Fe-Cr alloys

The toughness decrease induced by phase separation in Fe-Cr was first noticed by Becket (Becket, 1938). At that time, the underlying mechanism of the '475°C Embrittlement' was still unknown. Later, Fisher et al. (Fisher et al., 1953) detected the precipitation of Cr-rich

phase by X-ray diffraction which showed that the precipitate had the lattice parameter equal to that of a Fe-70Cr alloy. Furthermore, Williams & Paxton (Williams & Paxton, 1957) confirmed that the '475°C embrittlement' was due to the formation of Cr-rich precipitates (α') which can increase the hardness whilst decreasing the ductility of the materials. It is noteworthy that Williams & Paxton (Williams & Paxton, 1957) were the first ones to propose the existence of a miscibility gap in the Fe-Cr system, as shown in Fig. 2.4.

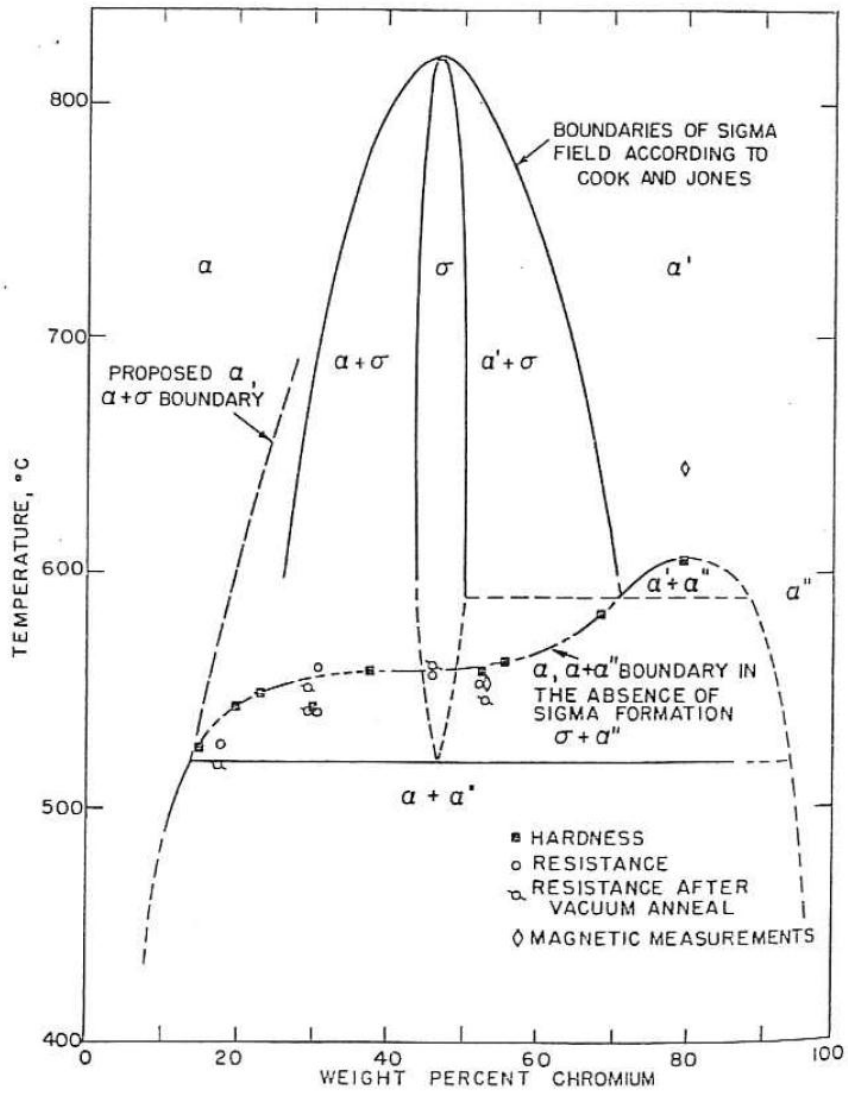

Figure 2.4 Partial phase diagram of the Fe-Cr system (William & Paxton, 1957).

With the development of the theory of spinodal decomposition by Hillert (Hillert, 1956, 1961), Cahn & Hilliard (1958) and Cahn (Cahn, 1961) and the notorious deterioration due to the '475 Embrittlement', the phase separation in Fe-Cr alloys has gradually drawn a lot of attention from the materials science community owning to the wide application of ferrite-containing alloys in industry. Since the 1960s different techniques have been applied to study phase separation in the binary system of Fe-Cr. For instance, Chandra & Schwartz (Chandra & Schwartz, 1971) employed Mössbauer spectroscopy to investigate the phase separation in Fe-60Cr (at. %) alloys according to the fact that an absorption peak occurs in the paramagnetic environment which is corresponding to the Cr-rich domains, as shown in Fig.

2.5; Later, Grobner (Grobner, 1973) observed the precipitates of α' phase by electron microscopy in the stainless steel of Fe-18Cr-2Mo (wt. %); Okada et al. (Okada et al., 1978) used transmission electron microscopy (TEM) to characterize the morphology of phase separation in the alloy of Fe-31Cr-23Co (wt. %), as shown in Fig. 2.6; Miller et al. (Miller et al., 1982, 1995) successively employed atom probe field ion microscopy (APFIM) and atom probe tomography (APT) to study the morphology of the phase separation in ferritic steels; in addition, small-angle neutron scattering (SANS) was adopted to investigate the phase separation in Fe-Cr alloys (Fe-20at. %, 35at. % and 50at. %Cr) by Bley (Bley, 1992), as shown in Fig. 2.7.

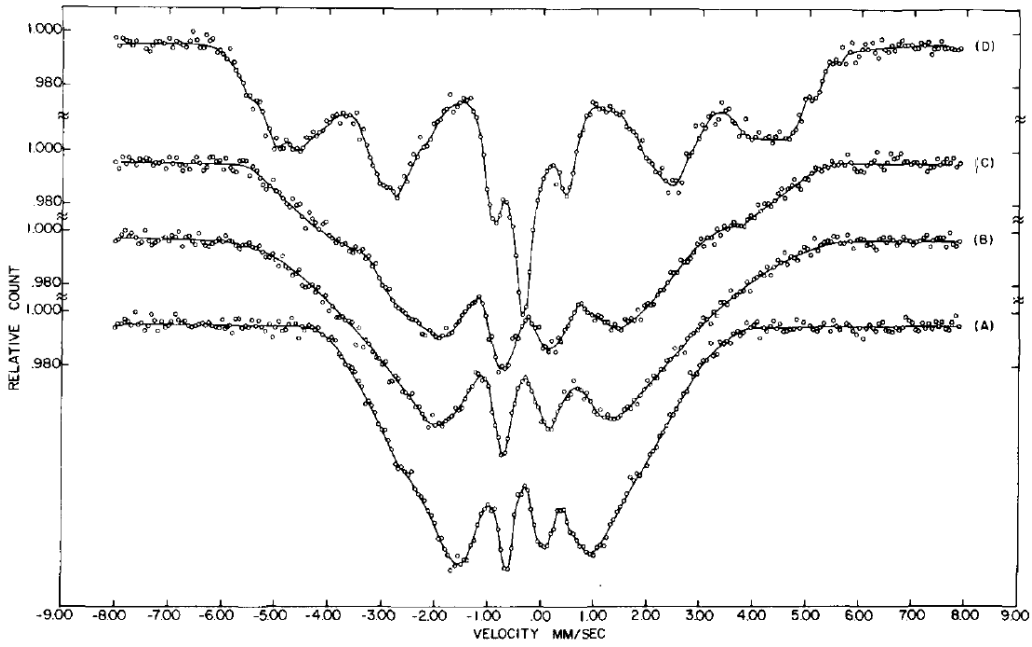

Figure 2.5 Mössbauer spectra of Fe-60Cr measured at room temperature: (a) the as-quenched alloy; the same alloy aged at 475 ℃ for (b) 30h; (c) 80h; (d) 1300h (Chandra & Schwartz, 1971).

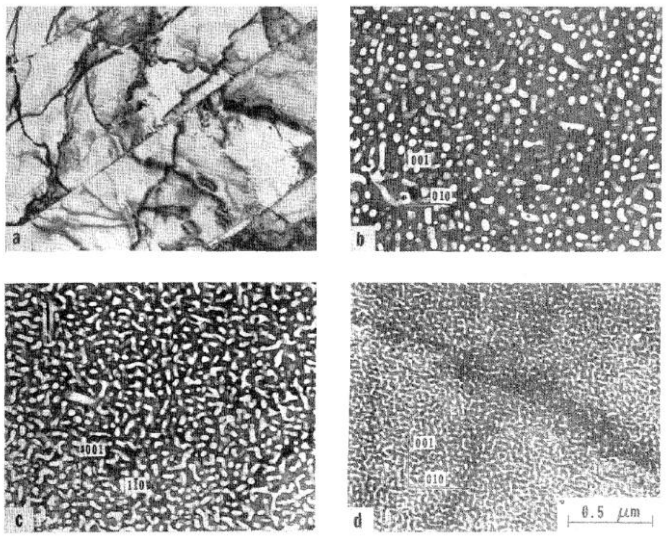

Figure 2.6 Bright field images of Fe-31Cr-23Co alloy aged for 1h: (a) at 680 ℃; (b) at 670 ℃; (c) at 660 ℃; (d) at 650 ℃ (Okada et al., 1978).

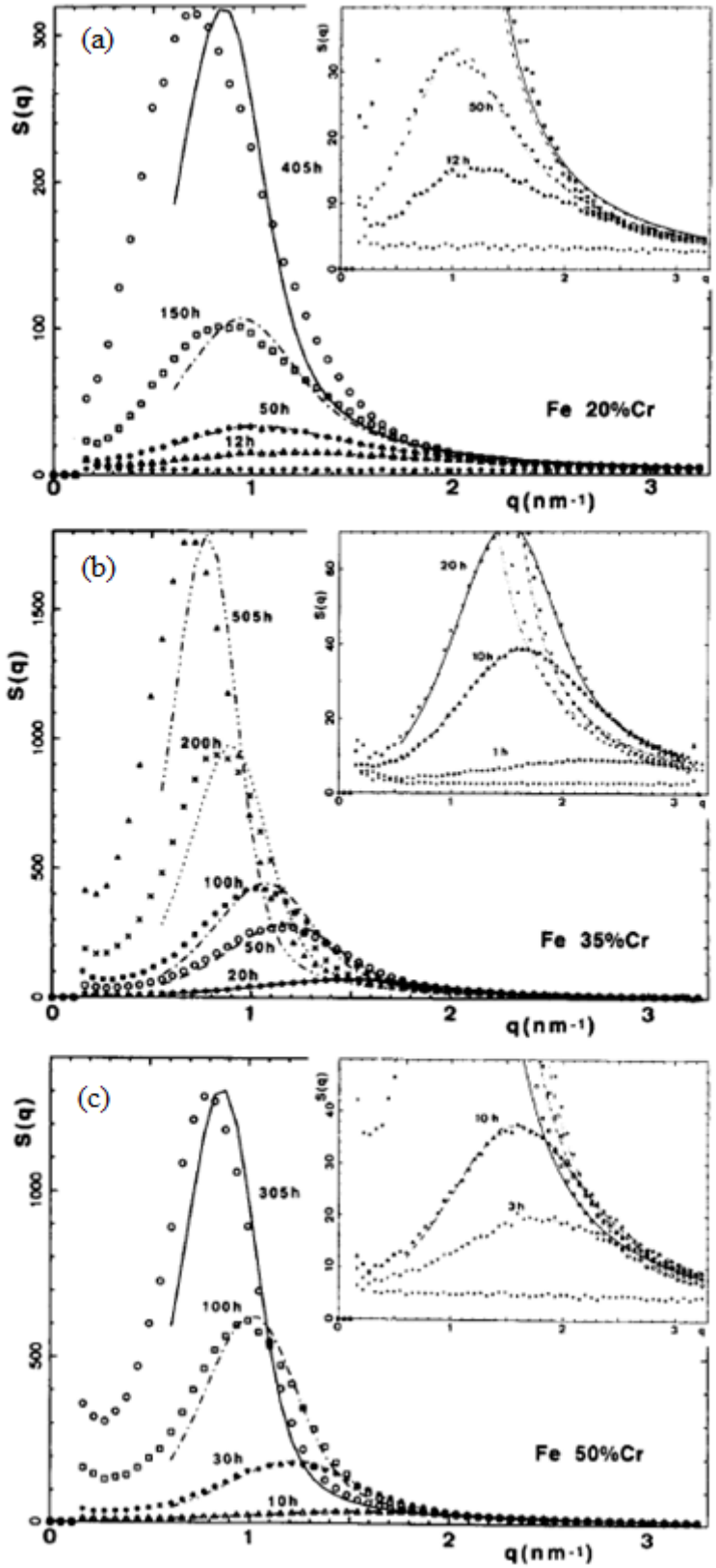

Figure 2.7 Experimental values of the structure factor in: (a) Fe-20 at. %Cr, (b) Fe-35 at. %Cr, (c) Fe-50 at. %Cr (Bley, 1992).

Chapter 3

Atom Probe Tomography and Its Application

Atom probe tomography is a powerful technique to study the local distribution of atoms in a small volume, e.g. 200x80x80nm^3. It has been successfully applied to study a wide range of materials, such as e.g. semi-conducting materials, steels and aluminum alloys. In this chapter, a short review of the development of atom probe tomography is presented, and then followed by a description of the application of atom probe tomography for investigating the phase separation in Fe-Cr based alloys.

3.1 Field ion microscopy

In 1935, Müller invented a new type of microscope based on the idea of the quantum mechanical tunneling found by Oppenheimer (Oppenheimer, 1928), which has been published later in 1936 (Müller, 1936). This new type of microscope was the starting point for the development of atom probe tomography. After two decades, in 1955, Müller developed the prototype of the microscope and successfully applied field emission to image atoms for the first time, see Fig. 3.1. This was called field ion microscopy (Müller, 1956). The process of field ion image formation is shown schematically in Fig. 3.2. At the beginning, the image gas atoms are approaching the surface of the positively charged specimens, as shown in process (a) in Fig. 3.2; due to the high electrical field around the specimen, the image gas atoms get polarized, as shown in process (b); thus, the image gas atoms are attracted to the specimen, in process (c); then the image gas atoms make a series of collisions close to the specimen, in process (d); during the collisions, the image gas atoms become thermally accommodated to the cryogenic temperature of the specimen, in process (e); finally, the image gas atoms are ionized with the positive charge and radially repelled from the specimen towards the imaging screen and produce a spot of light, in process (f). Therefore, the distribution of spots on the phosphor screen forms the field ion image (Miller, 2000). One example is the image of a body centered cubic (bcc) tungsten specimen obtained by field ion microscopy, as shown in Fig. 3.3, in which different poles are marked (Miller, 2000).

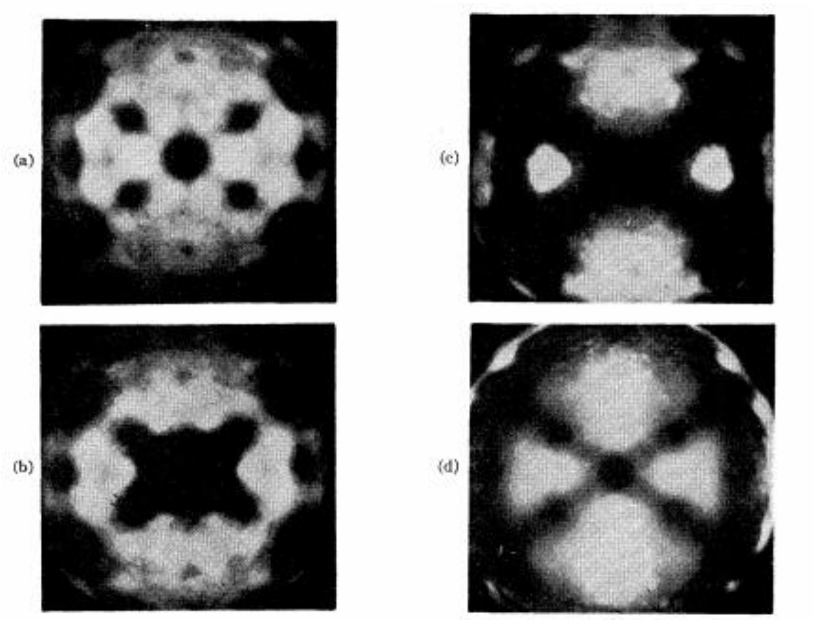

Figure 3.1 Field emission microscope pattern of tungsten (Müller, 1956)

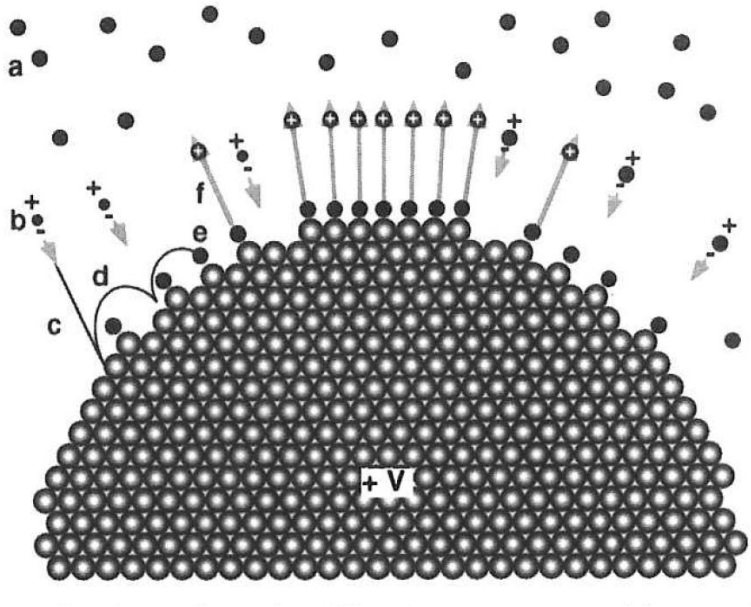

Figure 3.2 Process of field ion image formation (Miller, 2000)

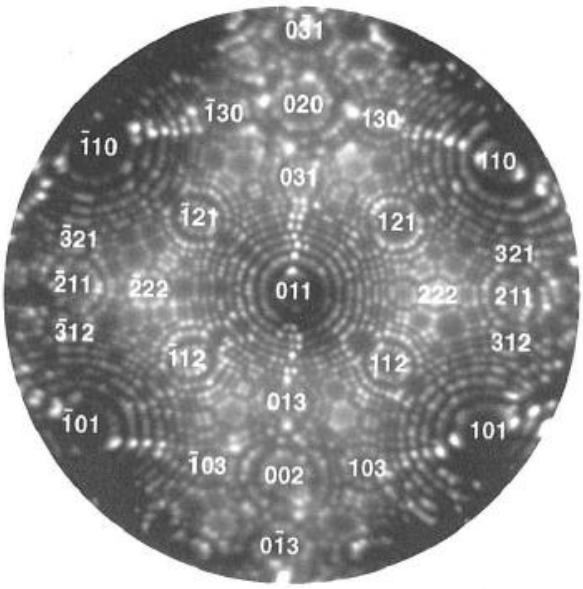

Figure 3.3 An indexed field ion micrograph of a body centered cubic tungsten specimen (Miller, 2000)

3.2 Atom probe field ion microscopy

In order to detect and identify the atoms evaporated from the specimen tip, Müller and Panitz (Müller & Panitz, 1967) in 1967, and Müller et al. (Müller et al., 1968) in 1968, introduced a new instrument: atom probe field ion microscope, which is a combination of a field ion microscope and a mass spectrometer, as shown in Fig. 3.4.

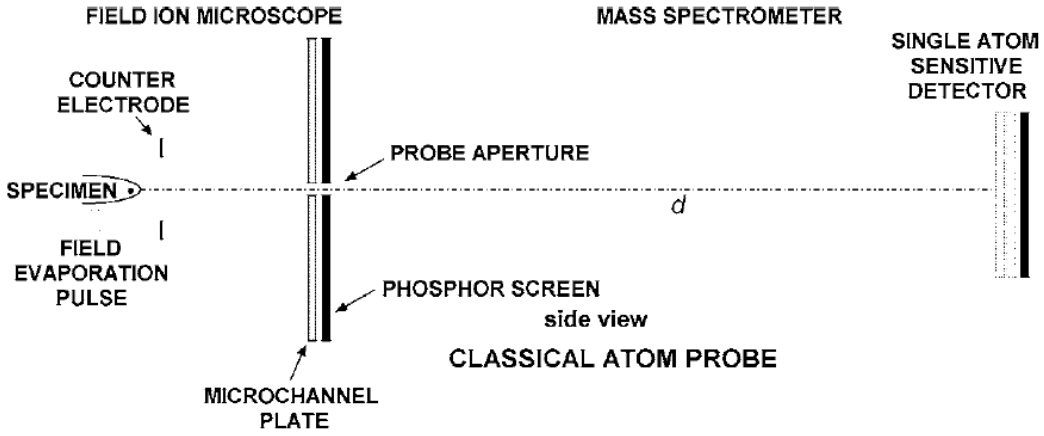

Figure 3.4 Schematic diagrams of the original atom probe field ion microscope (Kelly & Miller, 2007)

After the process of field evaporation, the atom with the charge of *n* on the surface of the specimen is accelerated up by the applied field. Thus, the potential energy of *neV* is converted into kinetic energy of $\frac{1}{2}mv^2$. Therefore, the mass-to-charge ratio *m/n* of the evaporated ion can be given by Eq. 3.1.

$$\frac{m}{n} = \frac{2e}{d^2}(V_{dc} + \alpha V_{pulse})t^2 \tag{3.1}$$

Where *e* is the charge of an electron; *d* is the distance between the specimen and the detector, as shown in Fig. 3.4; V_{dc} is the standing voltage; V_{pulse} is the pulse voltage amplitude; *t* is the time of flight from the specimen tip to the detector, which can be determined with a time-to-digital converter. This method is called time-of-flight mass spectrometry, which is used to determine the mass-to-charge ratio and thus identify the elements. During the standing voltage, no atoms should be evaporated; the ions are only field evaporated from the specimens during the applied pulse voltage.

Thus, both the standing voltage and pulse voltage should be selected appropriately according to different materials and analyzing temperatures. In general, the amplitude of the pulse voltage is 15%-20% of the standing voltage (Miller, 2000). More strictly, all these parameters including the amplitude of the pulse voltage, the standing voltage and the specimen temperature should be selected to make sure that all different atoms in the specimen should have the similar possibility to be evaporated during the application of the pulse voltage. Otherwise, it will lead to biased compositions since one of these elements evaporates between the pulses, and thus the composition of the element is lower than what it should be. The effect is shown in Fig. 3.5.

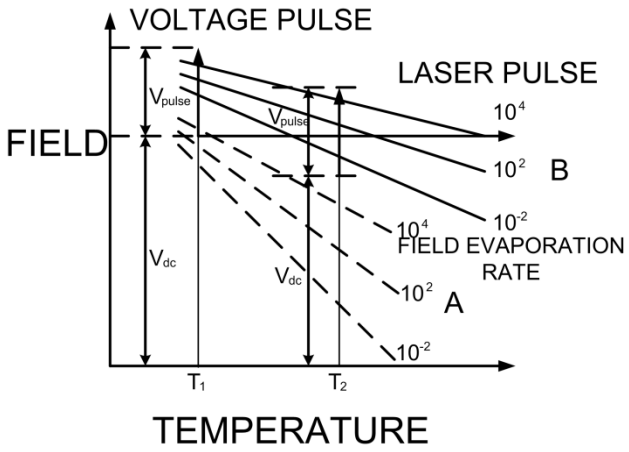

Figure 3.5 Evaporation field for two different elements at different temperatures (Miller, 2000)

3.3 Three-dimensional atom probe

In the 1980s, a new type of instrument was developed to be able to produce three-dimensional images of the internal structures by combining the position-sensitive detection with the time-of-flight mass spectrometry. The technique behind these 3-dimensional atom probe instruments were given the name, atom probe tomography (APT), as shown in Fig. 3.6. Different detectors have been invented to meet the requirements of the three-dimensional atom probe, such as optical atom probe (OAP) (Miller, 1991), position-sensitive atom probe (PoSAP) (Cerezo et al., 1988) and tomographic atom probe (TAP) (Bostel et al., 1989), as shown in Fig. 3.6.

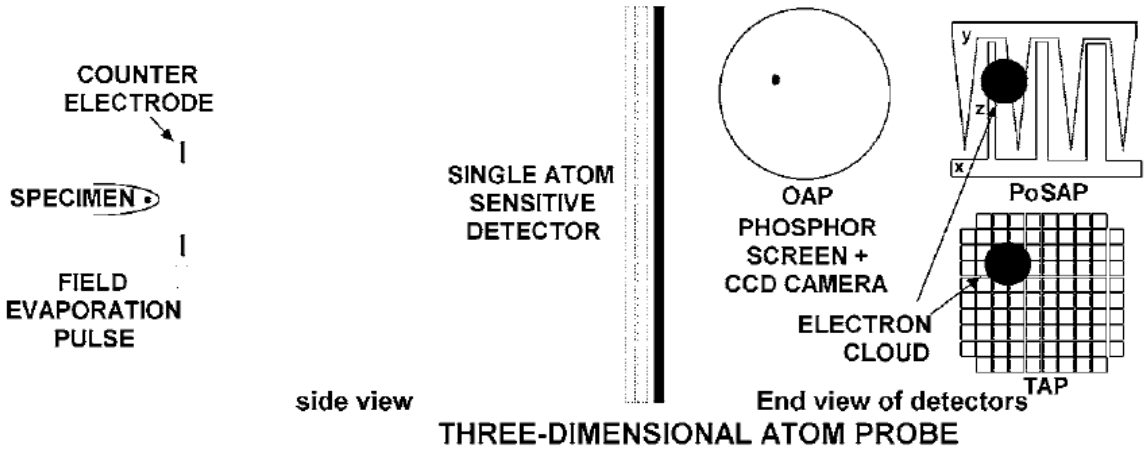

Figure 3.6 Three-dimensional atom probe with different detectors (Kelly & Miller, 2007)

Although the three-dimensional atom probe is a milestone in the development of atom probe tomography to reconstruct 3D structures of the specimen, there are two significant issues which hindered the application of three-dimensional atom probe in practice: 1) the low mass resolution due to the small energy deficit which arises because ions are evaporated at different times during the high voltage pulse; 2) very low data collection efficiency: the data collection rate is around 10 atoms/s or 10^6 atoms/day, which corresponds to an analyzed depth of 15-25nm/day.

In order to improve the mass resolution, the development of energy compensation by a reflectron lens was successfully applied on the three-dimensional atom probe (Warren et al., 1998), as shown in Fig. 3.7.

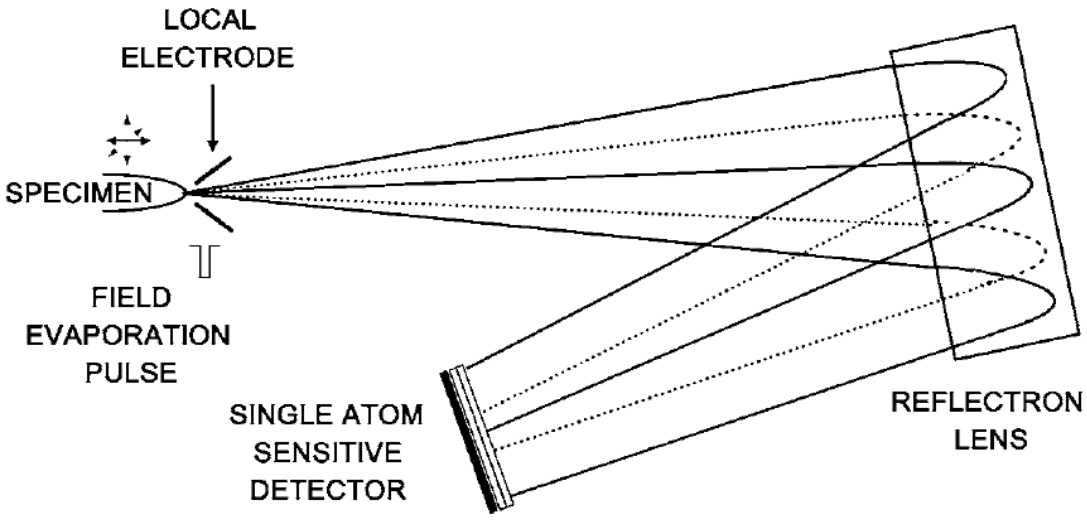

Figure 3.7 Three-dimensional atom probe with an energy-compensating reflectron lens (Kelly & Miller, 2007)

With the application of a reflectron lens on the three-dimensional atom probe, the mass resolution has been improved to a very good extent and can easily identify the isotopic atoms,

as shown in Fig. 3.8, in which different isotopic peaks can be evidently separated, such as Fe, Cr, Ni from the spectrum of the alloy Fe-26wt. %Cr-5wt. %Ni (Cerezo et al., 1998).

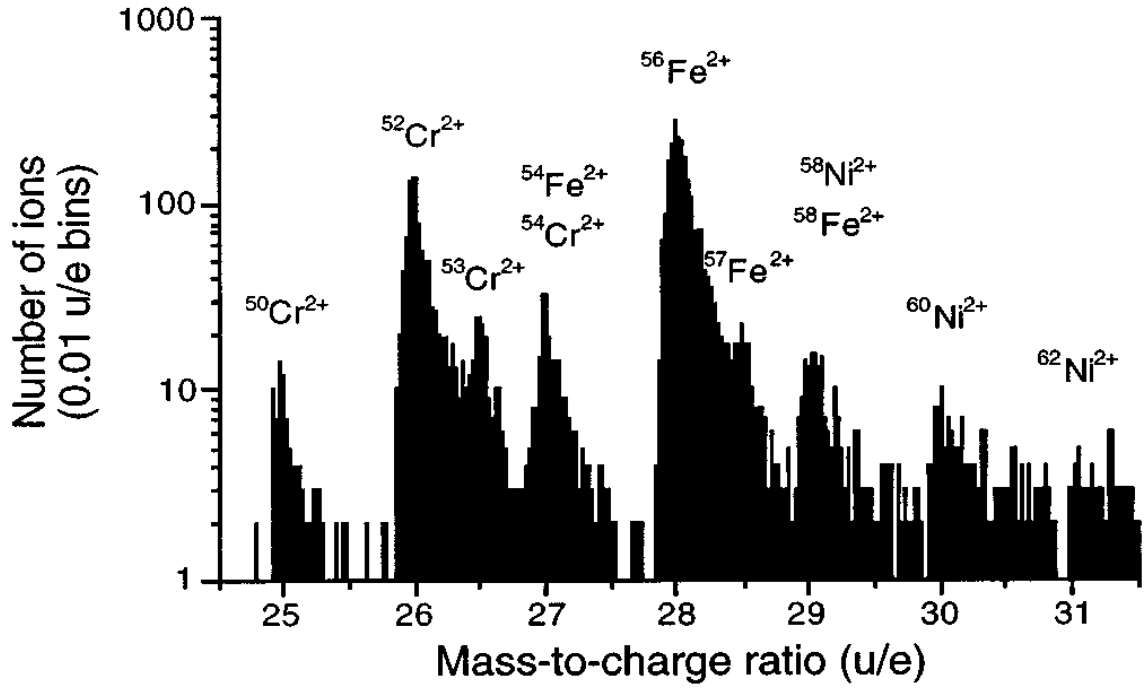

Figure 3.8 A spectrum of the alloy Fe-26wt. %Cr-5wt. %Ni (Cerezo et al., 1998)

3.4 Local electrode atom probe (LEAP)

Today's atom probe tomography instrument is named as local electrode atom probe (LEAP) by the company of Imago Scientific Instrument (nowadays, CAMECA). The first generation of commercial LEAP was constructed by Kelly and Larson, and the prototype LEAP is shown in Fig. 3.9(a). The latest version of LEAP is LEAP 4000X, which is shown in Fig. 3.9(b).

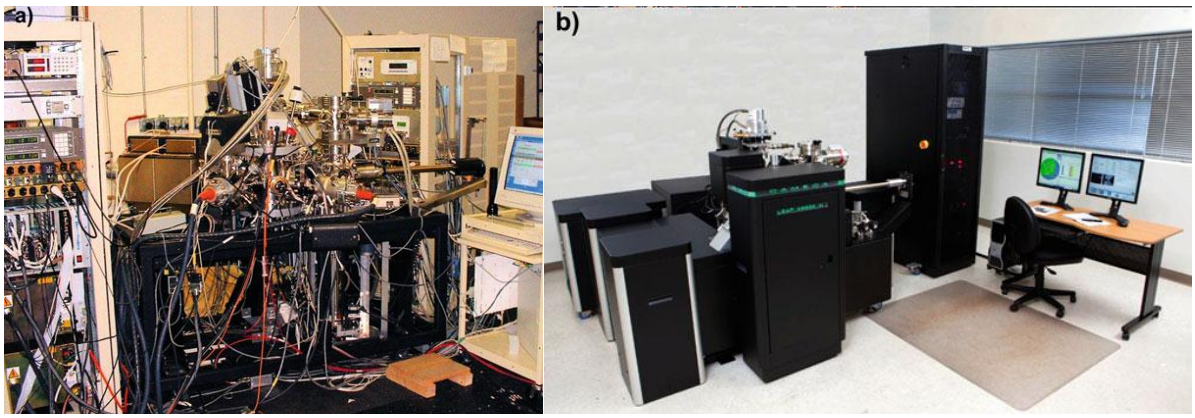

Figure 3.9 (a) Prototype of the commercial LEAP; (b) LEAP 4000X (Larson et al., 2013)

The new instrument was equipped with a local-electrode geometry comparing with the three-dimensional atom probe, as shown in Fig. 3.10. With the local electrode, the field has been enhanced up to 1.5 times or more. Thus, a lower applied voltage could produce the same field as in the three-dimensional atom probe. This type of field enhancement has two significant

improvements: 1) the local electrode could be applied to lower the applied voltage, thus, a higher data collection rates can be obtained; 2) due to the applied voltage decrease, there exists a relative reduction in the energy spread which could probably improve the mass resolution over the entire field of view (Kelly, et al., 1996). In principle, the combination of the local-electrode geometry has improved the data collection rate and the mass resolution over a large field of view in atom probe tomography (Larson et al., 2013).

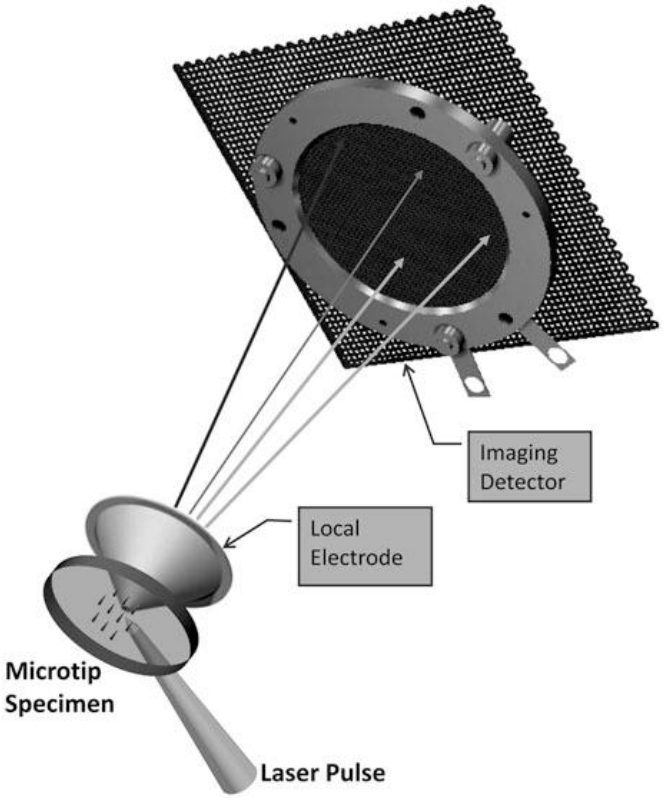

Figure 3.10 Schematic of LEAP with local electrode and detector geometry (Larson et al., 2013)

3.5 Application of APT to phase separation in Fe-Cr alloys

Atom probe tomography has been demonstrated to be a very useful technique to study the nano-scaled structures of materials due to the atomic-level spatial resolution after over fifty years of development. Due to this significant feature, APT has showed a huge potential to characterize the composition difference in nano-structures.

The application of atom probe tomography on the phase separation in Fe-Cr based alloys can be dated to the 1980s and was of great importance to directly observe the structures of phase separation. For instance, Brenner et al. (Brenner et al., 1984) observed the interconnected microstructures in Fe-28.5Cr-10.6Co (wt. %) aged for 8 hours at 600℃ by field ion microscopy, see Fig. 3.11. The white regions in the image represent the Fe-rich domains whereas the dark regions are the Cr-rich domains. Miller et al. (Miller et al., 1995) employed the position-sensitive atom probe to reconstruct the morphology and furthermore compared the results with modeling results. Danoix et al. (Danoix et al., 2004) investigated the hardening mechanism of duplex stainless steels aging at 400℃ by atom probe tomography.

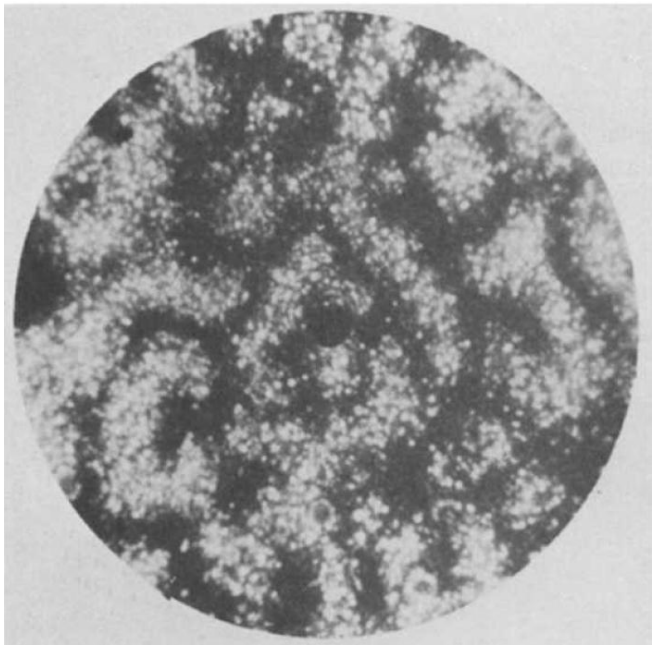

Figure 3.11 Field ion image of Fe-28.5Cr-10.6Co aged for 8 hours at 600 ℃ (Brenner et al., 1984)

Recently, Xiong et al. (Xiong et al., 2011) employed APT to determine experimentally the position of the spinodal line at 500 ℃ in Fe-Cr binary alloys. As can be seen in Fig. 3.12, the alloy with the composition of 26.65 at. % Cr shows isolated nuclei in the atom map of Cr (Fig. 3.12(a)), and the composition of the alloy thus seems to be located between the miscibility gap and the spinodal line. The experimental data is compared with a new thermodynamic evaluation of the phase diagram as can be seen in Fig. 3.12(d). This indicates that the mechanism is via nucleation and growth. For the alloy with the composition of 37.76 at. % Cr, the structures from the atom map of Cr in Fig. 3.12 (c) are interconnected, which indicates the mechanism is via spinodal decomposition. The results are in good agreement with the phase diagram in Fig. 3.12 (d). For the composition of 31.95 at. %Cr which is located quite close to the spinodal line, both nuclei and interconnected structures can be found in the atom map of Cr in Fig. 3.12 (b).

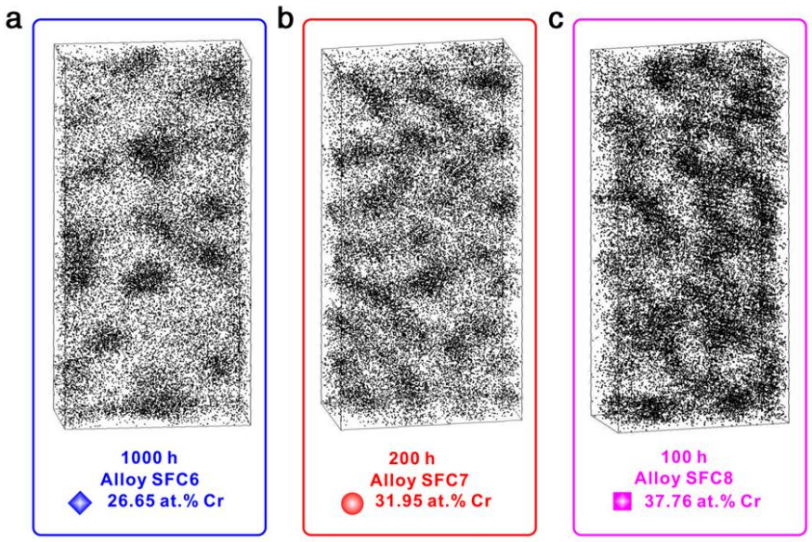

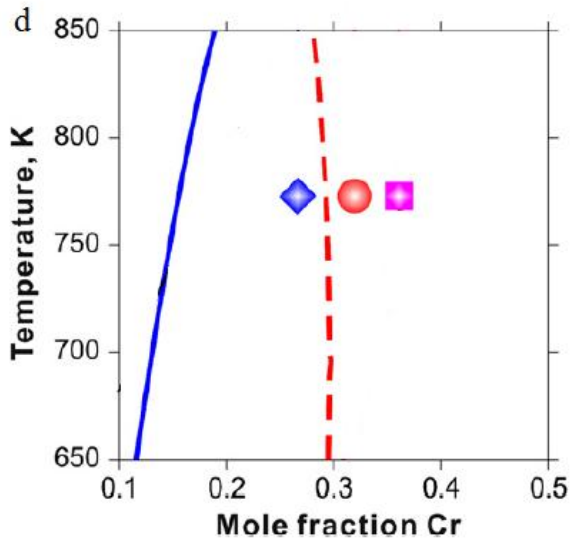

Figure 3.12 Atom maps of the Cr distribution for alloys with (a) 26.65 at. %, (b) 31.95 at. %, (c) 37.76 at.% Cr determined by APT, (d) zoomed-in phase diagram (the blue solid line is the miscibility gap and the red dashed line is the spinodal line). The size of the box for analysis is $30 \times 15 \times 6$ nm^3. (Xiong et al., 2011)

3.5.1 Sample preparation

In order to have a sharp-shaped tip to be analyzed, several methods have been developed for sample preparation in the latest several decades, mainly including electro-polishing and ion milling. In this section, two widely-used methods will be briefly introduced, i.e. two-step electro-polishing and focused ion beam (FIB).

Two-step electro-polishing

This method is based on the double-layer electro-polishing technique. The samples should be cut into blanks with the size of about 20mm×0.3mm×0.3mm. Afterward, the blank should be electro-polished using an electrolyte suitable for the investigated materials, as shown in Fig. 3.13(a). In the first step of electro-polishing, the top surface of the electrolyte has the strongest polishing rate. Thus, the electrolyte should be moved up and down in order to form a neck in the middle part of the sample. Then another more dilute electrolyte is used to obtain the final tip that can be analyzed in LEAP, as shown in Fig. 3.13(b). Usually, the tip has an angle of less than 15 °.

For the Fe-Cr based alloys in the present work, the recipe of the electrolyte in the first step is 10% perchloric acid, 20% glycerol and 70% methanol floating on the top of trichlorotrifluoroethane, and 2% perchloric acid in 2-butoxyethanol in the second step.

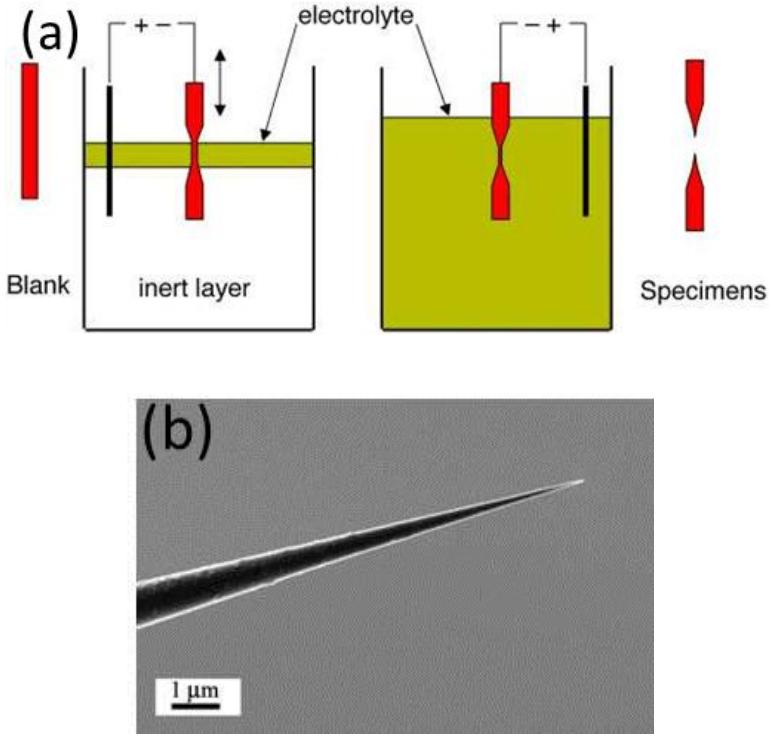

Figure 3.13 Sample preparation by electro-polishing: (a) two-step electro-polishing; (b) the final tip analyzed by LEAP (Andrén, 2011).

Focused ion beam (FIB) milling

This application of focused ion beam milling to prepare specimens for field-ion microscopy was first proposed by Larson et al. in 1998 (Larson et al., 1998). The merit of this method is that it permits the process of milling to be monitored during the preparation of the specimen. More importantly, interesting regions could be selected to be analyzed in LEAP, such as grain boundaries. Two main approaches can be used to sharpen the specimen into a needle-shaped tip for evaporation. The first one is to use an annular pattern during the milling. The beam is kept parallel to the specimen axis, as shown in Fig. 3.14(a). This method is quite similar to a pencil sharpener.

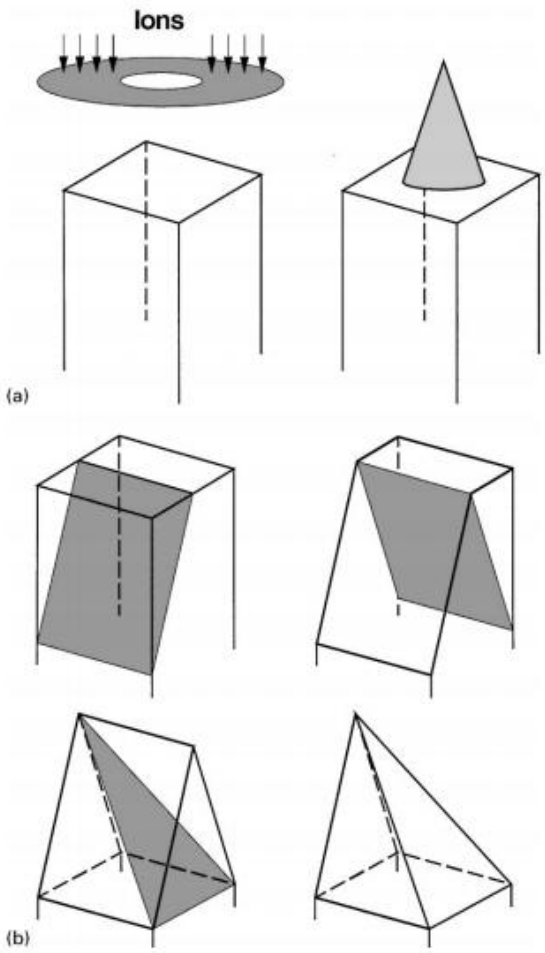

Figure 3.14 Schematic diagram showing methods of FIB milling using: (a) an annular pattern; (b) a cutting method (Larson et al., 1998)

3.5.2 Sample analysis by LEAP

The samples are placed in a high-vacuum chamber with a cooling system in order to meet the strict analysis environment in LEAP. The pressure is usually kept in the order of 10^{-11} torr to assure a good analysis. The temperature during analysis is highly dependent on the analyzed materials, and in the case of Fe-Cr alloys, the temperature is usually set between 20K and 80K to achieve similar evaporation rates for both Fe and Cr atoms. In the present work, the temperature was set to be 55K. Another important procedure before analysis is to align the tip with the electrode quite well. For a good alignment, the top of the tip should be located at the crossing point when one tries to extrapolate the edges of the electrode from the 2D image as shown by red dotted lines in Fig. 3.15.

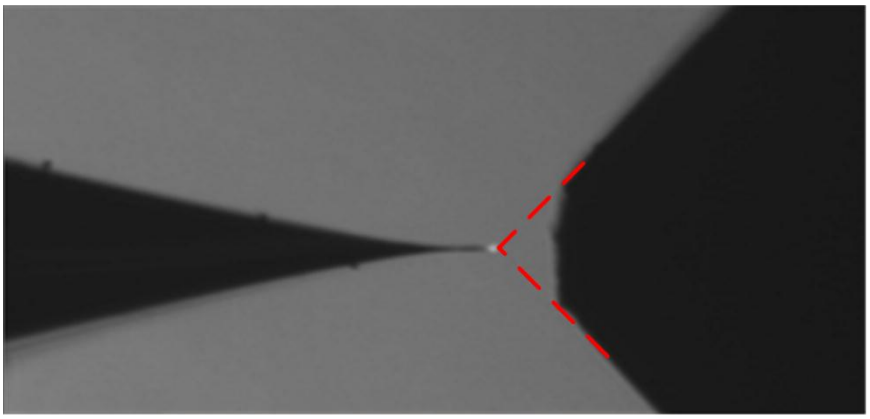

Figure 3.15 Alignment of the tip with the electrode

There are two kinds of analysis modes in LEAP, i.e. voltage mode and laser mode. Only conductive materials can be analyzed in the voltage mode and laser mode is very useful for non-conductive materials, such as ceramics.

At the beginning of the analysis, some phenomena may be found, such as oxidation that could form during the electro-polishing. Higher voltage is usually needed to remove the oxide layers. The voltage should be increasing slowly in order to avoid the fracture of the specimen during analysis.

3.5.3 Reconstruction by integrated visualization & analysis software (IVAS)

The reconstruction of the evaporated material in LEAP is performed by the integrated visualization & analysis software (IVAS). According to the data recorded by LEAP, the atoms were evaporated layer by layer which can be considered as 2D atom maps (x and y directions) at different z positions (Miller, 2000). Additionally, the positions of each evaporated ion in x and y directions were determined by the primary detector, and the time of flight for each atom has been recorded as well in order to generate the mass spectrum, and furthermore determine the type of each element. The basic idea of reconstruction process is to align different layers along the z direction to generate the 3D atom distribution.

In order to identify the atoms collected by the LEAP, the recorded mass spectrum is of significant importance, as shown in Fig. 3.8. In IVAS, users have to generate a suitable Range file to identify the corresponding mass-charge-ratio peaks in the mass spectrum when analyzing different alloy systems.

Particularly in IVAS, a smoothing method based on the moving average techniques has been adopted (Miller, 2000) when concerning the concentration. More importantly, IVAS has shown an impressive ability in dealing with clustering phenomena based on the maximum separation algorithm (Stephenson et al., 2007).

One example of the reconstructed specimens is given in Fig. 3.16.

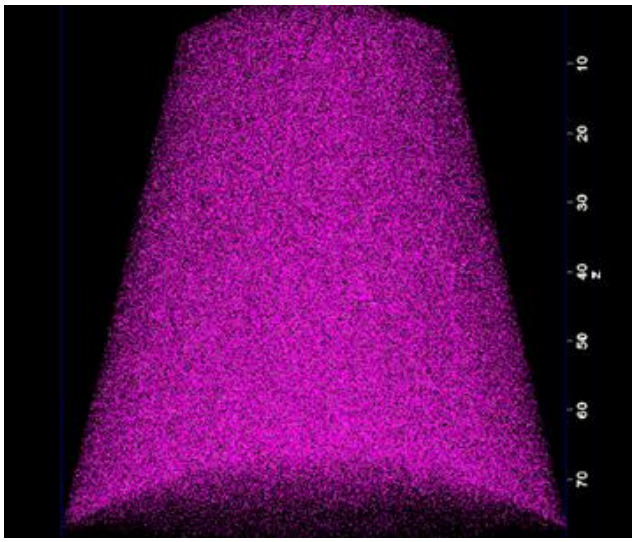

Figure 3.16 Reconstruction of the specimen

3.5.4 Measurement of wavelength

In order to attain the wavelength of phase separation in Fe-Cr alloys, several methods were proposed to approach the aim, for instance, auto-correlation function (Brenner et al., 1984), fast Fourier transform method (Odqvist et al, 2012) and radial distribution function (Zhou et al., 2013). In this section, only auto-correlation function will be introduced and the radial distribution function method will be presented in the next chapter.

Auto-correlation function

Based on the 1D concentration-field data from atom probe field ion microscope, Brenner et al. (Brenner et al., 1984) employed the auto-correlation function (ACF) to evaluate the wavelength of phase separation in Fe-Cr-Co alloy. The correlation coefficient from auto-correlation function is expressed in Eq. 3.2.

$$R_k = \frac{1}{\sigma^2} * \sum_{r=0}^{r_{max}-k} (C_i - C_0)(C_{i+k} - C_0) \tag{3.2}$$

Where, C_r and C_{i+k} are the concentration of the i^{th} and $i+k^{th}$ sample blocks; C_0 is the average composition; k is the lag; σ^2 is the variance of the composition of C_i, given by $\sigma^2 = \sum_{i=1}^{N}(C_i - C_0)^2$. In this case, the first maximum on the $R(k)$ curve is determined to be the wavelength .

In this method, the 1D concentration field was obtained first from either APFIM or APT, as shown in Fig. 3.17(a). Based on the 1D concentration profile, one can employ the auto-correlation function to obtain the curve of correlation coefficient and find the first maximum which is corresponding to the wavelength of phase separation. Later, Hyde et al. (Hyde et al., 1995) extended the 1D ACF method to 3D by using the radial concentration profile.

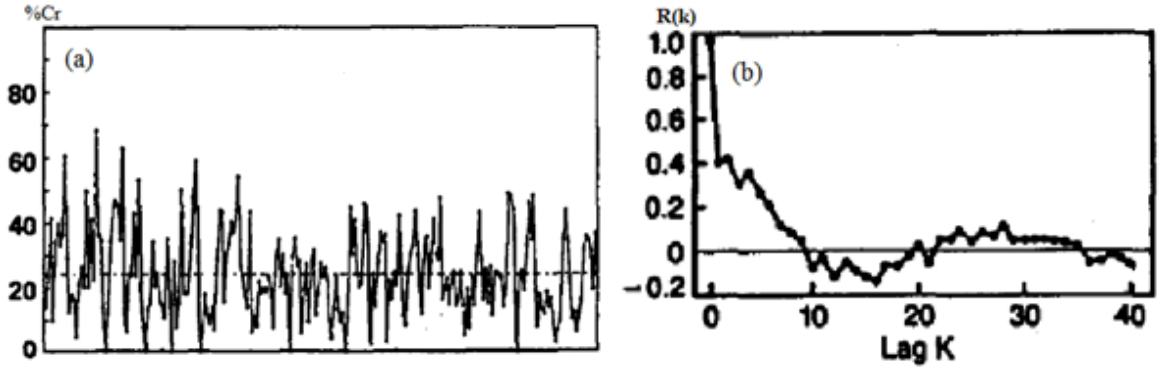

Figure 3.17 Alloy of Fe-26Cr-5Ni aged at 560 ℃ (a)1D concentration field profile with the block of 50 ions; (b) Auto-correlogram from the 1D concentration profile (Brenner et al., 1984).

3.5.5 Measurement of amplitude

With respect to the amplitude, there are several methods available at present: Langer-Bar-on-Miller (LBM) method (Langer et al., 1975), Variation method (Blavette et al., 1988), P_a method (Sassen et al., 1987; Godfrey et al., 1988; Brown et al., 1990) and RDF method (Zhou et al., 2013).

LBM method

The LBM method is the most widely used method nowadays to obtain the amplitude of phase separation. This method is based on the so-called frequency diagram. The frequency diagram is representing the composition frequency which is generated by using a box of fixed size to go through the whole volume of the specimen and calculate the frequency of different compositions. One example is given in Fig. 3.18. The dots represent the frequency diagram. The binomial distribution stands for the ideal distribution in a homogenized alloy. Once the phase separation proceeds, the peak of the distribution becomes lower and the width at the bottom of the distribution becomes wider since two phases with high Fe and Cr contents respectively occur.

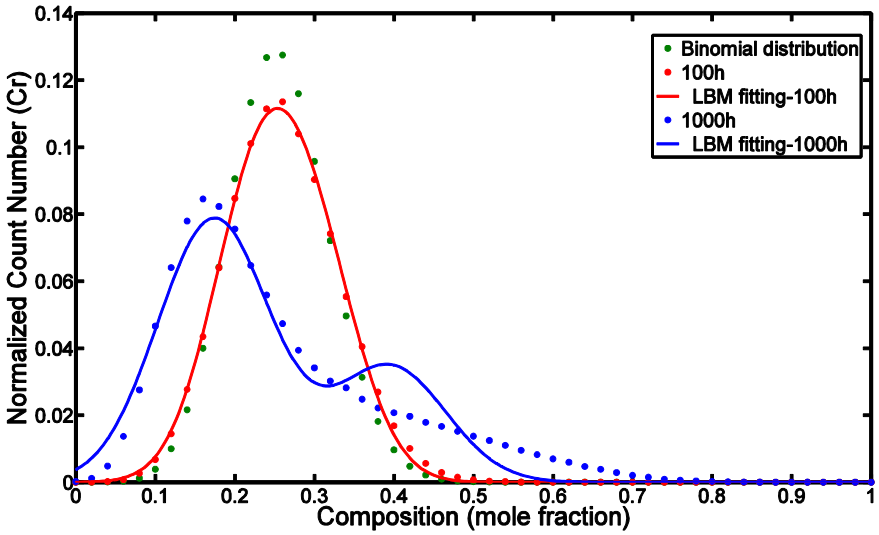

Figure 3.18 Frequency diagram for Fe-25Cr (block size 50 atoms)

Since the alloy is decomposed to Fe-rich phase (α) and Cr-rich phase (α') during aging at intermediate temperatures, the idea of the LBM method is to deconvolute the frequency diagram into two Gaussian distribution functions where one is for the Fe-rich phase (α) and the other is the Cr-rich phase (α'). The deconvolution of the frequency diagram is based on Eq. 3.3.

$$\rho(x) = \frac{1}{(2\pi*\sigma^2)^{1/2}} * \left\{ \frac{\mu_2}{\mu_1+\mu_2} * exp(-(x-\mu_1)^2/2\sigma^2) + \frac{\mu_1}{\mu_1+\mu_2} * exp(-(x-\mu_2)^2/2\sigma^2) \right\} \quad (3.3)$$

Where, μ_1 and μ_2 are the peak and trough compositions respectively; σ^2 is the variance of the Gaussian distributions. So the amplitude can be obtained by the subtraction between μ_2 and μ_1.

The solid lines in Fig. 3.14 are fitted according to the experimental frequency diagrams and obtained from Eq. 3.4. It can be easily seen that for more pronounced phase separation, i.e. long-term aged specimen, the fitting is not so good (the solid blue line in Fig. 3.22). More importantly, it has been pointed out from a recent paper (Zhou et al., 2013) that the amplitude obtained by the LBM method does not give accurately estimate the amplitude of the phase separation. In fact, this method underestimates the amplitude.

Variation method

The variation method is also based on the frequency diagram. As explained above, the peak of the distribution becomes lower and the width at the bottom of the distribution becomes wider when the phase separation occurs in the alloys. The variation method measures the absolute difference between the binomial distribution and the experimental frequency distribution, as defined in Eq. 3.4.

$$V = \sum_{i=0}^{N_b} |O(i, N_b) - B(i, N_b)| \quad (3.4)$$

Where O is the observed experimental distribution, B is the binomial distribution. Theoretically, the parameter of V can be varying between 0 and 2. The larger V value, the more pronounced phase separation occurs in the alloy. Thus, the method can simply compare the extent of the phase separation in different alloys, but cannot give the amplitude of the phase separation.

P_a method

The P_a method is based on the assumption of the sinusoidal concentration field of spinodal decomposition from Cahn (Cahn, 1961). The concentration field due to fluctuation is in the form of (Sassen et al., 1987; Miller, 2000):

$$p_j = c_0 + P_a \left[\frac{2\pi j}{m_d}\right], (0 \le j \le m_d) \quad (3.5)$$

Where, $2P_a$ is the peak-to-trough amplitude of the spinodal decomposition; c_0 is the mean solute concentration and m_d is the discretization of the composition profile. Usually, the value of m_d is chosen to be larger than 20.

According to statistics, the possibility of obtaining i solute atoms in a block containing N_b atoms is given by Eq. (3.6) as follows.

$$P(i, N_b) = \frac{1}{m_d} \sum_{j=0}^{m_d-1} \binom{N_b}{i} p_j^i q_j^{N_b-1} \tag{3.6}$$

Where $q_i = 1 - p_i$. Thus, the possibility can be maximized by finding the best fitting of S with the respect to P_a by stepping through all the possible values of P_a, as shown in Eq. (3.7).

$$S = \log|L| = \sum_{i=0}^{N_b} O(i) \log|P(i, N_b)| \tag{3.7}$$

Where $O(i)$ is the number of times a block with i solute atoms was observed.

Chapter 4

Connections between Phase Separation and Mechanical Properties

In order to characterize the phase separation in Fe-Cr alloys, different techniques have been found to detect the phase separation. Regarding the mechanical properties, hardness test and impact energy test are two effective methods since the phase separation in ferrite causes a hardness increase and impact energy drop in ferrite-containing stainless steels.

Although Becket (Becket, 1938) observed the hardness increase and ductility drop during the aging of stainless steels, the mechanism of hardening was not discovered until Fisher et al. detected the formation of Cr-rich phase (α') by X-ray examinations, which shows that the precipitation of α' should be responsible for the phenomenon of '475°C Embrittlement' in ferritic stainless steels.

Later, Cahn theoretically explained the hardening mechanism by spinodal decomposition and claimed that it was due to the internal stresses induced by the spinodal decomposition that could hinder the migration of dislocation analogous to the influence by precipitation hardening (Cahn, 1963). More importantly, he claimed that the hardening extent should be proportional to the square of the amplitude during spinodal decomposition. In addition, Park et al. (Park et al., 1986) investigated the phase separation in Fe-30wt. % Cr alloys and modeled the hardening mechanism based on Cahn's theory as well and discussed the aging-hardening phenomenon during aging. Regarding the experiments, Danoix et al. (Danoix et al., 2004) studied the connections between the hardness increase and the amplitude of phase separation during aging by atom probe tomography, and found that the hardness increase is in good accord with the extent of the phase separation that is represented by V values, as shown in Fig. 4.1. The experimental results are good evidence of the theory proposed by Cahn (Cahn, 1963) for the hardening mechanism by spinodal decomposition.

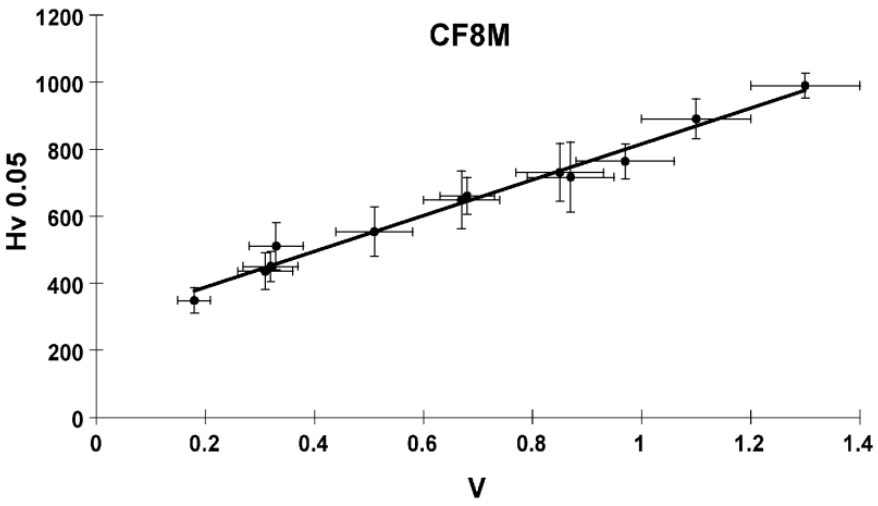

Figure 4.1 Extent of phase separation (V values) vs. hardness increase in CF8M (Danoix et al., 2004)

Recently, Capdevila et al. (Capdevila et al., 2008) investigated the hardening mechanism by hardness test and APT analysis. They compared the hardness increase with the size of α' and composition amplitude of phase separation respectively (see Fig. 4.2), and concluded that the hardness increase is more related to the composition amplitude instead of the size of α'. This is consistent with the previous discussion by Cahn (Cahn, 1963) and Danoix et al. (Danoix et al., 2004).

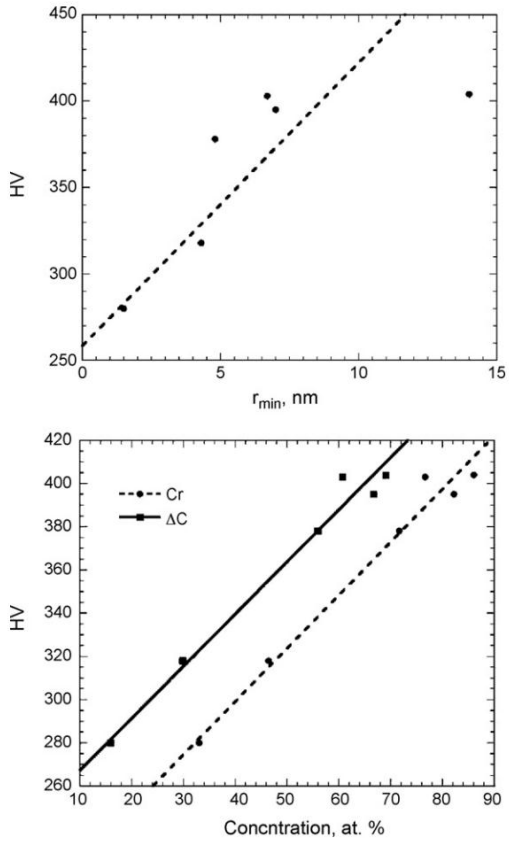

Figure 4.2 Linear relationship between hardness and the size and chromium content of the phase (Cr, dashed line) and composition amplitude (ΔC, solid line) (Capdevila et al., 2008).

Additionally, it is generally accepted that the hardening by the mechanism of spinodal decomposition is more pronounced than that of nucleation and growth since the spinodal decomposition has a finer microstructure.

Regarding the brittleness induced by the phase separation in Fe-Cr alloys, the possible reason could be due to the formation of the Cr-rich phase which deforms in a brittle manner similar to the pure Cr alloy (Miyazaki et al., 1974). While phase separation occur the impact toughness changes from ductile to brittle, as shown in Fig. 4.3.

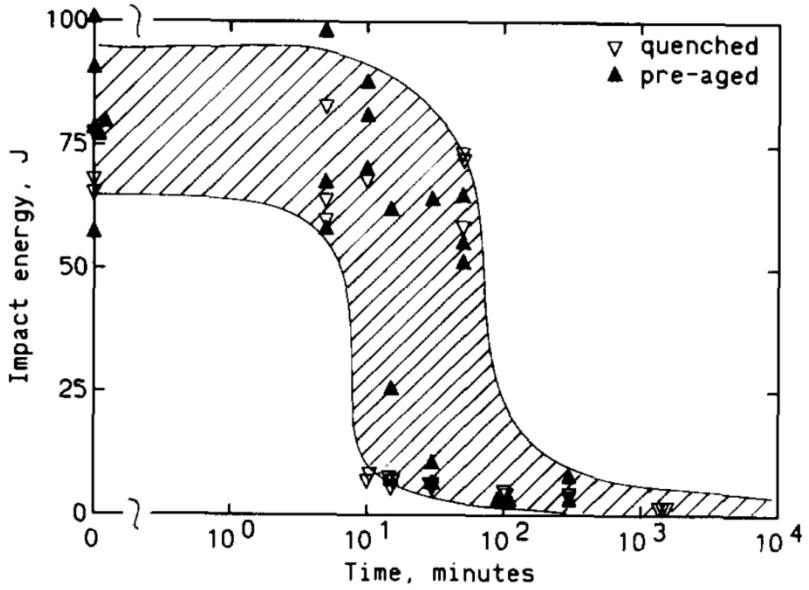

Figure 4.3 Charpy V-impact energy vs. aging time at 475 ℃ (Cortie & Pollak, 1995)

Besides the phase separation, some other concurrent phenomena have also been reported to be responsible for the embrittlement, such as Cu clusters (Thuvander et al., 2012) and G-phase (Zhou et al., 2012).

Chapter 5

Methodologies

In this chapter, details regarding the RDF analysis from atom probe tomography data and mechanical tests will be presented, including the principle of quantitatively evaluating the wavelength and amplitude by the RDF method in the phase separation of Fe-Cr alloys, hardness measurements and Charpy-V impact energy tests.

5.1 Radial distribution function

A new method based on the radial distribution function (RDF) has been put forward recently to evaluate the wavelength of phase separation in Fe-Cr alloys (Zhou et al, 2013). RDF analysis was employed to represent the radial concentration profile starting from every detected atom of the chosen element. Thus it indicates the probability density of finding an atom *j* at r when an atom *i* is the origin (De Geuser et al., 2006; Miller & Kenik, 2004). In the RDFs presented here, 0.2 nm was taken as the step size. The measured concentration at each position was normalized with respect to the average bulk concentration. The RDF can be expressed as in Eq. (5.1).

$$RDF(r) = \frac{C_E(r)}{C_0} = \frac{N_E(r)/N(r)}{C_0} \tag{5.1}$$

Where $C_E(r)$ is the atomic composition of element E at the distance of r, C_0 is the average composition of element E in the analyzed volume, $N_E(r)$ is the total number of atoms of element E at the distance of *r*, $N(r)$ is the total number of atoms of all elements at the distance of *r*. The generation of RDF curves is schematically shown in Fig. 5.1. It should be mentioned that each atom of the selected element is chosen as the center atom and the RDF curve gives the normalized average composition at certain distances. Thus, the RDF curves show very good statistical results. Similar to the auto-correlation function, the first maximum on the RDF curve represents the wavelength of phase separation in investigated alloys.

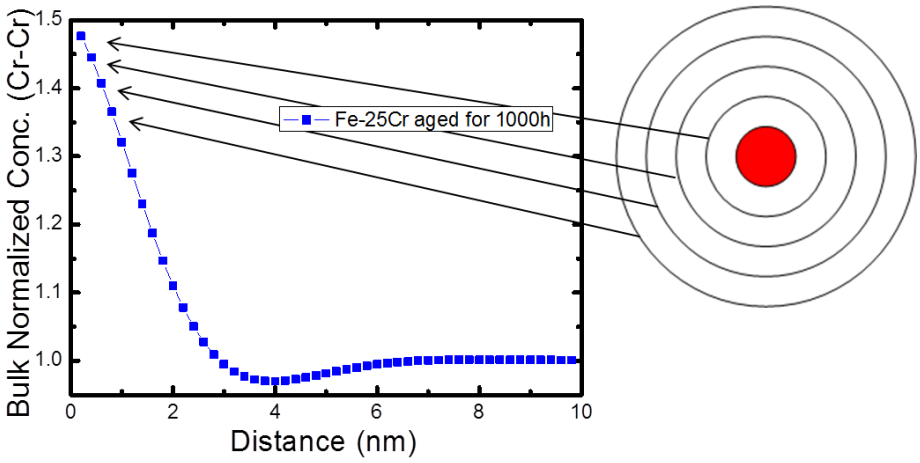

Figure 5.1 Generation of a RDF curve

5.2 Wavelength evaluation by RDF

In order to interpret the meaning of RDF curves, two RDF curves generated from the Cr-rich domain and Cr-depleted domain respectively are depicted in Fig. 5.2. The RDF curves were generated by only choosing the Cr atoms in one Cr-rich domain and on Cr-depleted domain as the centers, respectively. An obvious maximum can be found on the RDF curve generated from Cr-rich region, which can be interpreted so that the nearest Cr-rich domains were approached as the distance increases from the chosen Cr atoms. In fact, this is the definition of wavelength that represents the distance between the nearest two Cr-rich domains. Additionally, there usually exists a minimum on the RDF curve as well, which can be interpreted as the nearest Cr-depleted regions were approached. Importantly, it is consistent that the location of the first minimum is at the half distance of the first maximum. Similarly, the minimum and maximum on the RDF curve generated from the Cr-depleted region can be interpreted in the same way. Moreover, the RDF curve generated from the Cr-rich domain has a very strong positive interaction at the short distances; on the contrary, the RDF curve from the Cr-depleted domain has a negative interaction at short distances.

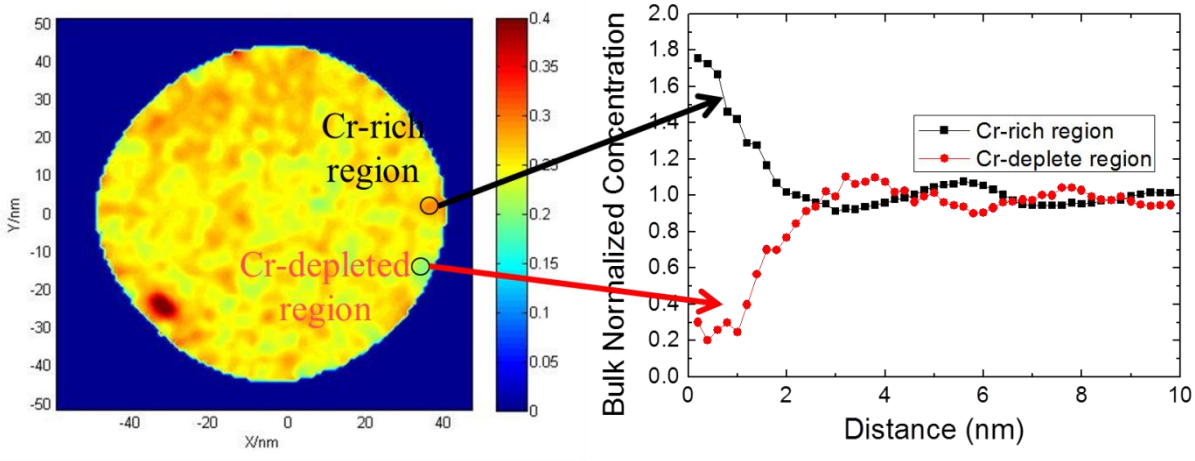

Figure 5.2 RDF curves from Cr-rich and Cr-depleted regions

Assuming that the volumes of the Cr-rich domains and Cr-depleted domains are equal, there are much more Cr atoms in the Cr-rich domains due to the high content of Cr in these domains. Therefore, the positive interaction at short distances generated from Cr-rich domains on the RDF curves will dominate when a statistical analysis of RDF is generated by choosing all the Cr atoms as the center. This is the reason why the extent of the positive interaction at short distances indicates the degree of the phase separation in Fe-Cr alloys. Additionally, the first maximum on the RDF curve gives the information of average distance between two nearby Cr-rich domains if the first maximum exists. It has been noticed that the more pronounced phase separation, the easier to find the first maximum on the RDF curve. As can be seen in Fig. 5.3, the first maximum can be found in most cases in which the phase separation is pronounced. Furthermore, the first minimum is located at the half distance of the first maximum, which is consistent with the previous discussion.

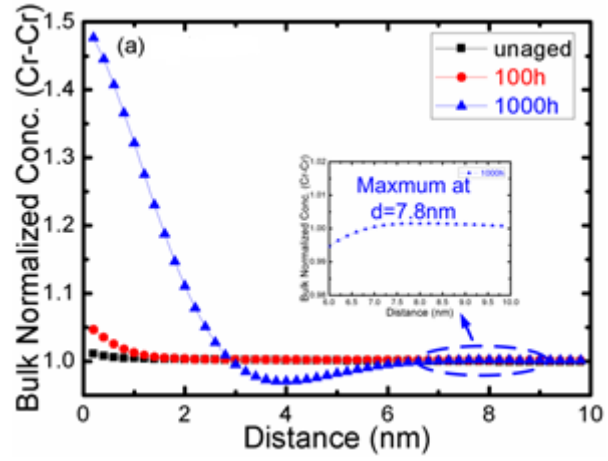

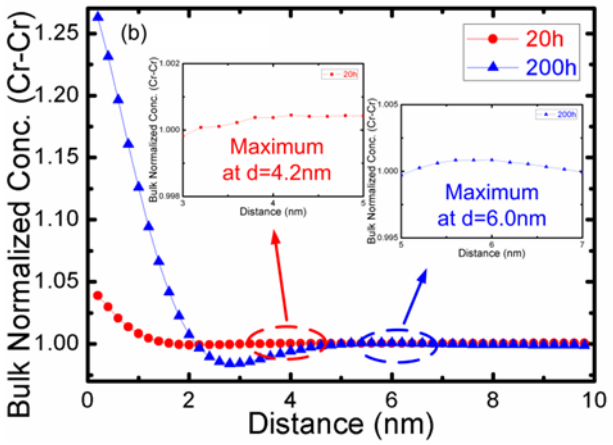

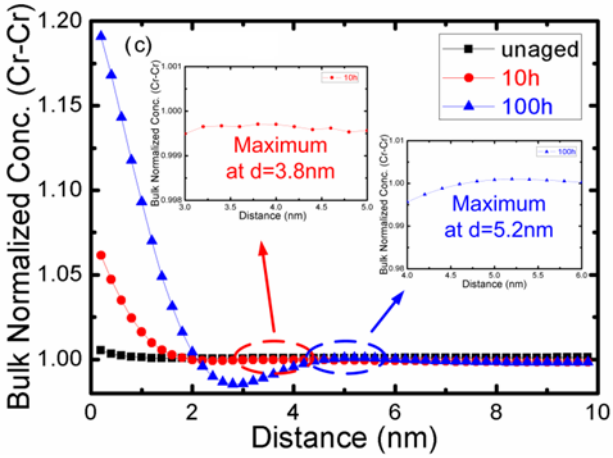

Figure 5.3 RDFs from three investigated materials aged at 500 ℃ (a) Fe-25Cr (b) Fe-30Cr (c) Fe-36Cr.

Nevertheless, there exist some RDF curves without the maximum, such as the RDF curve of the alloy with the composition of Fe-25Cr aged at 500 ℃ for 100h. A more general treatment can be helpful to find the wavelength in the less decomposed alloys. More details can be found in **Paper I**.

5.3 Amplitude evaluation by RDF

The method based on RDF curves to evaluate the amplitude of the phase separation was proposed by Zhou et al. in 2013 (Zhou et al., 2013). The process of obtaining the amplitude by RDF method is schematically given in Fig. 5.4. In order to obtain the amplitude, it is of great significant to select the domains which can stand for the peak and trough values of the assumed sinusoidal composition profile. In principle, the wavelength can be easily obtained by the RDF curve. Based on the wavelength, a simple assumption was made to evaluate the number of Cr-rich domains: all the Cr-rich domains are located in the center of the cube with the length of the wavelength and all the cubes are placed side by side as a crystal structure. Thus, the number of the total Cr-rich domains (or Fe-rich domains) can be estimated by Eq. (5.2). By the help of the iso-surface tool in IVAS, the number of Cr-rich domains (or Fe-rich domains) can be selected by choosing a suitable threshold value to obtain the exact quantity of Cr-rich domains (or Fe-rich domains) obtained by Eq. (5.2). The selected Cr-rich domains were shown in Fig. 5.5. The two RDF curves were generated in the selected Cr-rich domains and Fe-rich domains respectively to find the peak composition and valley composition of the assumed sinusoidal concentration field, as shown in Fig. 5.6. With these two compositions, the amplitude can be simply obtained by the subtraction of these two values.

$$N = \frac{V}{\lambda^3} \tag{5.2}$$

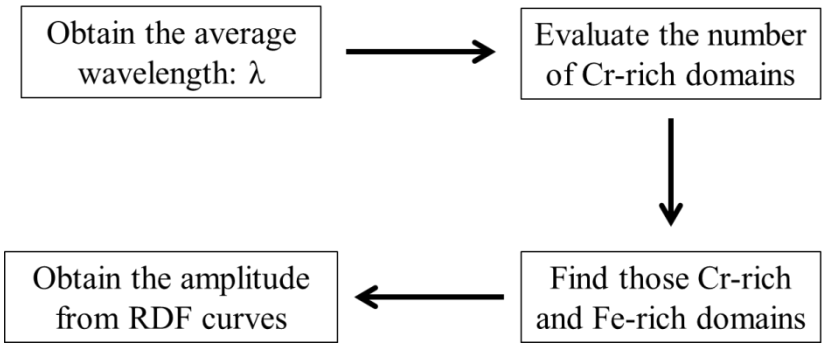

Figure 5.4 Process of the RDF method

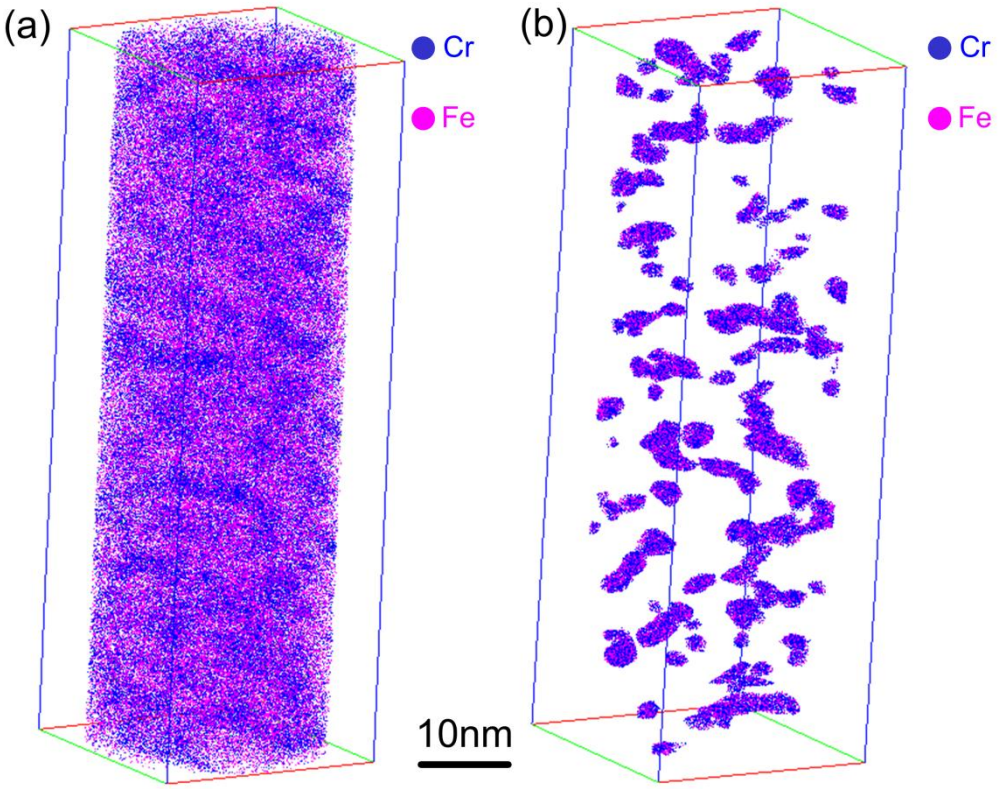

Figure 5.5 Atom maps of Fe-25Cr aged for 1000h at 500 ℃: (a) Cylinder of 80nm*27nm, (b) Selected Cr-rich domains by iso-surface in IVAS

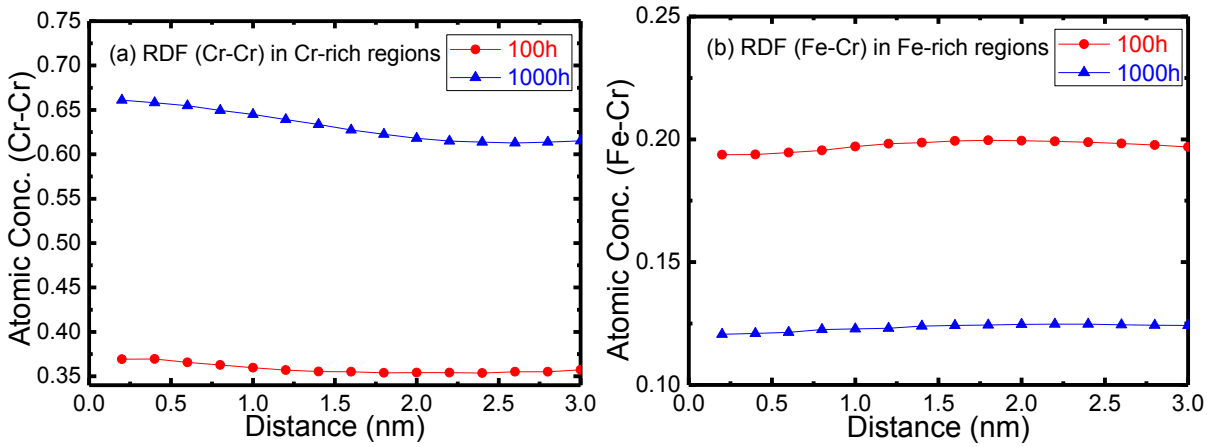

Figure 5.6 RDF of Cr-Cr for the alloy of Fe-25Cr in (a) Cr-rich regions; (b) Fe-Cr in Fe-rich regions

More importantly, a very simple equation (Eq. (5.3)) was derived to calculate the amplitude of phase separation based on the RDF curve according to the sinusoidal composition profile proposed by Cahn (Cahn, 1961). In this equation, the only unknown parameter is *RDF(0)*. In order to obtain the parameter of *RDF(0)*, we can extrapolate the RDF curve to the distance of 0 where *RDF(0)* is obtained. More details can be found in **Paper I**.

$$2A = 2C_0\sqrt{2(RDF(0) - 1)} \tag{5.3}$$

5.4 Mechanical properties tests

5.4.1 Hardness measurements

The hardness tests were performed on the micro-hardness machine. The chosen load in the present work was 100 grams. The load was applied for 20 seconds to make a quadrangular pyramid in the surface of the materials. In order to measure the values of the micro-Vickers hardness, two diagonal lines were drawn to evaluate the hardness of the material. Afterwards, the micro-hardness could be calculated automatically in the software of Leica according to the length of two diagonal lines. Ten measurements have been performed on each specimen to obtain good statistic results. Fig. 5.7 shows one example of hardness increase with aging time at 500 ℃.

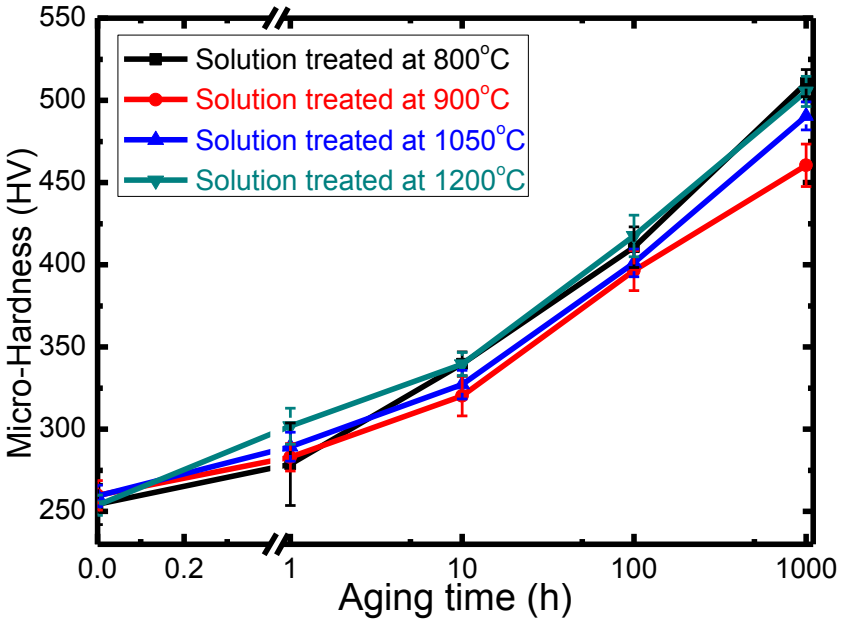

Figure 5.7 Hardness increase with aging time

5.4.2 Impact energy tests

The half-size Charpy-V notch impact energy was chosen to determine the toughness of the materials. The size of the samples for ductility tests is 55mm×10mm×5mm according to EN 10045. In order to avoid the influence of the oxidation on toughness tests after aging, the milling on the notch was used. One example of the test results is given here in Fig. 5.8, showing the ductile to brittle transition during aging at 500 ℃.

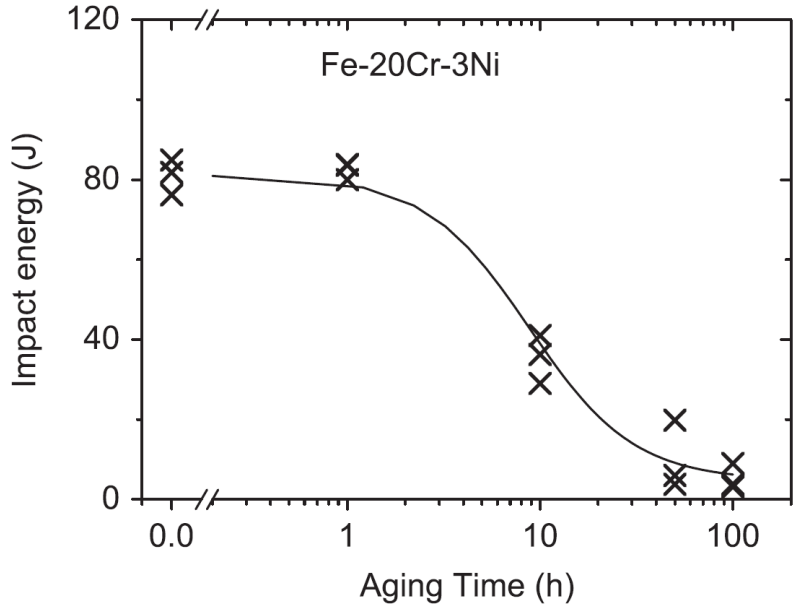

Figure 5.8 An example of half-size Charpy-V notch impact energy tests

Chapter 6

Summary of Appended Papers

Paper I. Quantitative evaluation of spinodal decomposition in Fe-Cr by atom probe tomography and radial distribution function analysis

The quantitative evaluation of wavelength and amplitude in spinodal decomposition was investigated in the present paper. A new method based on the radial distribution function (RDF) from atom probe tomography analysis was proposed to evaluate the wavelength and amplitude of phase separation in Fe-25Cr, Fe-30Cr and Fe-35Cr binary alloys. In addition, the results of wavelengths and amplitudes obtained by the RDF method have been compared with the wavelengths obtained by the auto-correlation function (ACF) and amplitudes obtained by the Langer-Bar-on-Miller (LBM) method respectively. Detailed evidence shows that the most common-used LBM method underestimates the amplitudes of phase separation in the binary alloys. The wavelengths obtained by the RDF curves have an exponential relation with aging time, which is consistent with the theory. But no such trend for the wavelengths obtained by 1D ACF could be found. Moreover, a very simple equation was derived to calculate the amplitude of phase separation which gives consistent amplitudes with those obtained by the RDF method.

Paper II. Observations of Cu clustering in a 25Cr-7Ni super duplex stainless steel during low temperature aging under load

Clustering of Cu was observed by atom probe tomography in the 25Cr-7Ni super duplex stainless steel after aging at 325 ℃ with an external tensile load. The observation shows that Cu clustering locates in the intermediate regions between Fe-rich domains and Cr-rich domains. From the RDF curve of Cu-Cu by atom probe tomography, the higher extensile load induces stronger Cu clustering. In addition, the Cu clustering was found to be one of the reasons to take responsibility for the low-temperature embrittlement of the supple duplex stainless steels of 25Cr-7Ni.

Paper III. Concurrent phase separation and clustering in the ferrite phase during low temperature stress-aging of duplex stainless steels

The motivation for this work was due to that the welding bead metals were found to be much more sensitive to the '475°C Embrittlement' than the base metals and the heat-affected-zone (HAZ) metals. Another aim was to investigate the influence of external tensile stress on the phase separation since duplex stainless steels often is used in load-bearing applications. The results based on the RDF curves from atom probe tomography showed that the phase separation in the welding bead metals is much more pronounced than that in the base metals and the HAZ metals. The bright field images from transmission electron microscope showed that there exist much higher density of dislocations in welding bead metals than in the other two metals. The high density of dislocations should take the responsibility for the more severe '475°C Embrittlement' found in welding bead metals since dislocations can facilitate the diffusion process, and thus increase the phase separation in welding bead metals. Additionally, the external tensile load was found to increase the phase separation as well. The reason being that the external tensile stress can enhance the diffusion, and thus favor both phase separation and cluster formation. In addition, clusters of Ni-Mn-Si-Cu were detected in the intermediate regions of Fe-rich and Cr-rich regions by atom probe tomography. These clusters were considered to be precursors of G-phase. Cu was found to partition with the G-phase precursor clusters. It was proposed that the clustering of Ni-Mn-Si-Cu partly could be, alongside phase-separation, responsible for the '475°C Embrittlement' in the investigated materials.

Paper IV. Initial clustering - a key factor for phase separation kinetics in Fe-Cr based alloys

Initial clustering of Cr was found in the as-quenched specimens of different materials by the help of RDF curves from atom probe tomography analysis. In order to explain the formation of initial Cr clustering, austenite from the same material of 2507 duplex stainless steel has also been investigated by atom probe tomography. No initial clustering in austenite was observed, which excluded the possibility of thermal fluctuation at high temperature during homogenization. According to the comparison of the initial Cr clustering in materials with different Cr-contents, it was found that the extent of initial Cr clustering increases with increasing Cr-content. The reason for that is probably due to the phase separation when quenching into the miscibility gap. In addition, initial Cr clustering was not found in the nano-flex material because the composition of the material is located quite close to the miscibility gap, thus there should be almost no phase separation during quenching. Furthermore, phase field modelling was performed to predict the influence of the initial Cr clustering on the evolution of the phase separation. The results showed that the initial Cr clustering has an obvious effect on the morphology of the phase separation.

Paper V. The 475 ℃ embrittlement in Fe–20Cr and Fe–20Cr–X (X=Ni, Cu, Mn) alloys studied by mechanical testing and atom probe tomography

The aim of this work was to investigate the influence of the alloying elements i.e. Ni, Cu and Mn on the phase separation during aging at 500 ℃ compared to the binary Fe-Cr alloy. Micro-hardness tests, impact energy tests and atom probe tomography analysis were used to study the phase separation. According to the results of the Cr-Cr RDF curves, the addition of Ni and Mn significantly enhances the kinetics of the phase separation compared to the binary Fe-20Cr alloy, but Cu was found to have very little effect on the kinetics of phase separation. However, all three ternary alloys show stronger hardness increasing trend than the binary alloy, especially the ternary of Fe-Cr-Cu. The reasons are different for the different ternaries. In Fe-Cr-Ni and Fe-Cr-Mn, it is due to the phase separation which induces the hardening phenomenon; but in Fe-Cr-Cu, the Cu clusters should take the responsibility for the hardening during aging.

Paper VI. Direct atom probe tomography observations of concentration fluctuations in Fe-Cr solid solution

The concentration fluctuations were directly observed by the help of atom probe tomography in the solid solution alloy of Fe-46.5%Cr quenched from four different homogenization temperatures. Statistical analysis based on frequency diagram and radial distribution function shows the obvious evidence that there exist the atomic short-range order. Furthermore, the results based on the Monte Carlo simulations agree qualitatively well with the experimental results. In addition, more details show that the clustering tendency decreases with the homogenization temperatures above the miscibility gap. The present observation can provide the experimental data for taking the concentration fluctuations into account in the future phase field simulation.

Paper VII. Effect of homogenization temperature on subsequent spinodal decomposition during aging in Fe-46.5Cr

The influence of the homogenization temperature on the phase separation was investigated in the present paper. Two different homogenization temperatures (800 and 900 ℃) and their influence on the evolution of phase separation were studied. The results from the hardness measurements showed that the specimen solution-treated at the low (800 ℃) homogenization temperature has a stronger hardening trend than the other one. Data from tom probe tomography shows the consistent results that the specimen solution-treated at 800 ℃ has a more pronounced decomposed structure than that solution-treated at 900 ℃. The reason for this difference is as a consequence of the clustering formation above the miscibility gap.

Chapter 7

Concluding Remarks and Future Work

7.1 Concluding remarks

The efforts of the present thesis have been dedicated to increase the knowledge of the phase separation in ferrite-containing stainless steels since stainless steels are an important type of steels in practice. The focus of the present thesis includes: (1) a new method to evaluate the wavelength and amplitude of phase separation was proposed. In addition, some other phenomena can be analyzed by this method as well, such clustering and elements' partition. (2) The influence of different factors on the phase separation has been thoroughly investigated, such as the external tensile stress, dislocations, alloying elements, initial clustering and the homogenization temperatures.

Through the systematic investigation on the ferrite-containing stainless steels, several conclusions can be drawn:

- Atom probe tomography is a very useful technique to study the phase separation in Fe-Cr alloys and characterize the morphology. Radial distribution function is a very effective tool to detect the phenomena of phase separation, clustering and elements' partition.
- The Langer-Bar-on-Miller method was demonstrated to underestimate the amplitude of phase separation for early stages. The new method based on radial distribution function was proposed to be able to evaluate both the wavelength and amplitude of phase separation in Fe-Cr alloys. In addition, a simple equation was derived to calculate the amplitude, which is in good agreement with the results from the radial distribution function method.
- External tensile stress was found to enhance the phase separation in duplex stainless steels. High density of dislocations has significant influence on the phase separation due to the fact that the defects can facilitate the diffusion phenomenon and phase separation is diffusion-controlled process.
- Cr clustering was detected in the as-quenched specimens with the help of radial distribution function. The details show that this clustering comes from the phase separation when quenching into miscibility gap.
- The solution temperatures have significant influence on the evolution of phase separation. Cr clustering was found above the miscibility gap, which is in good agreement with the theory. More importantly, this Cr clustering plays a very important

role in the following aging at 500 ℃ and induces much more pronounced phase separation. In addition, the quenched-in vacancies have a significant influence on the evolution of phase separation due to that vacancies can facilitate the diffusion.

7.2 Suggestions on future work

Although the phase separation in Fe-Cr alloys has been studied for more than 70 years, there are still several challenges connected to this phenomenon. Some of these challenges are:

- In order to shed more light on the miscibility gap for high Cr Fe-Cr alloys more experimental work should be focused on these alloys.

- The critical temperature of the miscibility gap in the binary system of Fe-Cr is still undetermined by experiments. The difficulty in determining the critical temperature is that the driving force for phase separation could be negligible when the temperature goes close to the critical one of the miscibility gap. Thus the kinetics could be rather slow and the phase separation is difficult to detect at the temperatures close to the critical temperature.

- Additional experiments should be performed to understand the influence of alloying elements on the phase separation comparing to the pure binary of Fe-Cr. Several elements have been studied in ternary cases, for instance, Ni has been found to enhance the phase separation but the addition of Al seems to suppress the phase separation to some extent. However, the reasons for the influence of alloying elements on the phase separation are still unclear. It should be considered from the aspects of both thermodynamics and kinetics.

- There is an urgent need for the improvement of thermodynamics and kinetics databases in the ternary or even multi-component systems for materials design. New assessments on the thermodynamics database for ternaries are highly desired. In addition, the kinetics database at intermediate and low temperatures is especially lacking since most of these experiments were done at rather high temperatures.

- More experimental work should be performed for the in-situ study of the phase separation. With the help of modeling on phase separation by either Monte Carlo or phase field, the in-situ study of phase separation could be of significant importance to compare with the modeling to understand the mechanism under this phenomenon. Small-angle neutron scattering is the best solution at present for the in-situ study of phase separation in Fe-Cr alloys.

Acknowledgements

I would like to give all my thanks to all the coworkers and organizations which have contributed to this thesis work during my 4-year Ph. D study.

First of all, I would like to express my sincere gratitude to my main supervisor Professor John Ågren. Your comprehensive knowledge and professional scientific discussion are very helpful to me and my research life. I would like to give my deepest gratitude to my co-supervisor Docent Peter Hedström. Thank you so much for your patient guidance and significant effort during the periods of my graduate studies. I would like to give my great gratitude to my other co-supervisor Docent Joakim Odqvist. Your kind help and great effort on my work are sincerely appreciated.

I would like to thank Dr. Mattias Thuvander from the Department of Applied Physics in Chalmers University of Technology for your helpful guidance and great effort for me on atom probe tomography.

I would like to acknowledge Professors Staffan Hertzman and Jan-Olof Nilsson for your kind support and helpful suggestions on Spinodal Project within the Hero-m Center.

I would also like to acknowledge my colleagues from Department of Materials Science and Engineering at KTH for providing a great research atmosphere and inspiring discussions. A special thanks to Dr. Wei Xiong and Reza Naraghi for your help on Thermo-Calc and DICTRA, and Fei Huyan on the mechanical tests.

I would also like to thank the VINN Excellence Center Hero-m, VINNOVA, Swedish Steel Industry, KTH Royal Institute of Technology, ERASMUS MUNDUS TANDEM and Outokumpu Stainless Research Foundation for financial support for this work. As well as Stiftelsen för Tillämpad Termodynamik and Olle Erikssons stiftelse for travel grants.

Finally, I would like to express my greatest gratitude to my wife and my parents for their endless support.

Bibliography

Andrén H.O. (2011). Lecture notes of Chalmers APT course 2011.

Baur R & Gerold V (1962). The existence of a metastable miscibility gap in aluminium-silver alloys. Acta Metallurgica **10**, 637-645.

Becket F.M. (1983). On the allotropy of stainless steels. Transaction of the American Institute of Mining and Metallurgical Engineers **131**, 15-36.

Bernstein, I. M. (1977). Handbook of Stainless Steels. New York, NY: McGraw-Hill.

Blavette D., Grancher G. & Bostel A. (1988). Statistical analysis of atom-probe data (I): Derivation of some fine scale features from frequency distributions for finely dispersed systems. J. de Phys. **49-C6**, 433-438.

Bley F. (1992). Neutron small-angle scattering study of unmixing in Fe-Cr alloys. Acta Metall. Mater. **40**, 1505-1517.

Borgh I., Hedström P., Blomqvist A., Ågren J. & Odqvist J. (2014). Synthesis and phase separation of (Ti, Zr) C. Acta Materialia **66**, 209-218.

Bostel A., Blavette D., Menand A., Sarrau A. (1989). Toward a tomographic atom-probe. J. Phys. Paris, Colloq. **50**, C8-501-506.

Brenner S.S., Camus P.P., Miller M.K. & Soffa W.A. (1984). Phase separation and coarsening in Fe-Cr-Co alloys. Acta Metall. **32**, 1217-1227.

Brown J.E., Cerezo A., Godfrey T.J., Hetherington M.G. & Smith G.D.W. (1990). Quantitative atom probe analysis of spinodal reaction in ferrite phase of duplex stainless steel. Mater. Sci. Tech. **6**, 293–300.

Cahn J.W. & Hilliard J.E. (1958). Free energy of a nonuniform system: I. J. Chem. Phys. **28**, 258-267.

Cahn J.W. (1961). On spinodal decomposition. Acta Metall. **9**, 795-801.

Cahn J.W. (1963). Hardening by spinodal decomposition. Acta Metall. **11**, 1275-1282.

Capdevila C., Miller M.K., Russell K.F., Chao J. & González-Carrasco J.L. (2008). Phase separation in PM 2000™ Fe-base ODS alloy: Experimental study at the atomic level. Materials Science and Engineering A **490**, 277-288.

Cerezo A., Godfrey T.J. & Smith G.D.W.(1988). Application of a position-sensitive detector to atom probe microanalysis. Rev. Sci. Instrum. **59**, 862-866.

Cerezo A., Godfrey T.J., Sijbrandij S.J., Smith G.D.W. & Warren P.J. (1998). Performance of an energy-compensated three-dimensional atom probe. Review of scientific instruments **69**, 49-58.

Chandra D. & Schwartz L.H. (1971). Mössbauer effect study of the 475 °C decomposition of Fe-Cr. Metall. Trans. **2**, 511-519.

Cortie M.B. & Pollak H. (1995). Embrittlement and aging at 475 C in an experimental ferritic stainless steel containing 38 wt.% chromium. Materials Science and Engineering A **199**, 153-163.

Danoix F., Auger P. & Blavette D. (2004). Hardening of aged duplex stainless steels by spinodal decomposition. Microscopy and Microanalysis **10**, 349-354.

De Geuser F., Lefebvre W. & Blavette D. (2006). 3D atom probe study of solute atoms clustering during natural ageing and pre-ageing of an Al-Mg-Si alloy. Philos. Mag. Lett. **86**, 227–234.

Fisher R.M., Dulis E.J. & Carroll K.G. (1953). Identification of the precipitate accompanying 885 F embrittlement in chromium steels. Tran. AIME **197**, 690-695.

Godfrey T.J., Hetherington M.G., Sassen J.M. & Smith G.D.W. (1988). The characterization of spinodal structures in duplex CF3 steels. J. de Phys. **49**, 421–426.

Grobner P.J. (1973). The 885 °F embrittlement of ferritic stainless steels. Metall. Trans. **4**, 251-260.

Hall E. O. & Algie S. H. (1966). The sigma phase. Metallurgical Reviews **11**, 61-88.

Hillert M. (1956). A theory of nucleation for solid metallic solutions. Ph.D Thesis. MIT.

Hillert M. (1961). A solid-solution model for inhomogeneous systems. Acta Metall **9**, 525–535.

Holleck H. (1986). Material selection for hard coatings. Journal of Vacuum Science & Technology A **4**, 2661-2669.

Hyde J.M., Miller M.K., Hetherington M.G., Cerezo A., Smith G.D.W. & Elliott C.M. (1995). Spinodal decomposition in Fe-Cr alloys: Experimental study at the atomic level and comparison with computer models—II. Development of domain size and composition amplitude. Acta metallurgica et materialia **43**, 3403-3413.

Kasper J. S. (1954). The ordering of atoms in the chi-phase of the iron-chromium-molybdenum system. Acta Metallurgica **2**, 456-461.

Kelly T.F., Camus P.P., Larson D.J., Holzman L.M. & bajikar S.S. (1996). On the many advantages of local-electrode atom probes. Ultramicroscopy **62**, 29-42

Kelly T. F. & Miller M. K. (2007). INVITED REVIEW ARTICLE: Atom probe tomography. Review of Scientific Instruments **78**, 031101.

Langer J.S., Bar-on M. & Miller H.D. (1975). New computational method in the theory of spinodal decomposition. Phys. Rev. A **11**, 1417-1429.

Larson D.J., Foord D.T., Petford-Long A.K., Anthony T.C., Rozdilsky I.M., Cerezo A., & Smith G.W.D. (1998). Focused ion-beam milling for field-ion specimen preparation: preliminary investigations. Ultramicroscopy **75**, 147-159.

Larson D.J., Prosa T.J., Ulfig R.M., Geiser B.P. & Kelly T.F. (2013). Local Electrode Atom Probe Tomography. New York, US: Springer Science.

Larsson L.E. (1967). Pre-precipitation and precipitation phenomena in the Al-Zn system. Acta Metallurgica **15**, 35-44.

Meijering J.L. (1961). On the thermodynamics of the Au-Pt system. Journal of Physics and Chemistry of Solids **18**, 267-268.

Miller M.K., Brenner S.S., Camus P.P., Piller J. & Soffa W.A. (1982). Low-temperature precipitation in iron-chromium binary alloys. Proc. Int. Field Emiss. Symp. **29**, 489-496.

Miller M.K. (1991). Concepts in atom probe designs. Surf. Sci. **246**, 428-433.

Miller M.K., Hyde J.M., Hetherington M.G., Cerezo A., Smith G.D.W. & Elliott C.M. (1995). Spinodal decomposition in Fe-Cr alloys: experimental study at the atomic level and comparison with computer models-I. Introduction and methodology. Acta Metall. Mater. **43**, 3385-3401.

Miller M.K. (2000). Atom probe tomography: analysis at the atomic level. New York, US: Kluwer Academic/Plenum Publishers.

Miller M.K. & Kenik E.A. (2004). Atom probe tomography: A technique for nanoscale characterization. Microsc. Microanal. **10**, 336–341.

Miyazaki T., Nakagaki M. & Yajima E. (1974). Phase decomposition and 475℃ embrittlement in Fe-Cr and Fe-Cr-Co alloys. J. Japan Inst. Metals **38**, 70-77.

Müller E.W. (1936). Zh. Tekh. Fiz. **17**, 412.

Müller E.W. (1956). Field Desorption. Phys. Rev. **102**, 618-624.

Müller E. W. & Panitz J. A. (1967). Proceedings of the 14th International Field Emission Symposium, The National Bureau of Standards, Washington DC, (unpublished).

Müller E.W., Panitz J.A., & McLane S.B. (1968). The atom-probe field ion microscope. Rev. Sci. Instrum. **39**, 83-86.

Nilsson J. O. & Liu P. (1991). Aging at 400–600 °C of submerged arc welds of 22Cr–3Mo–8Ni duplex stainless steel and its effect on toughness and microstructure. Materials Science and Technology **7**, 853-862.

Odqvist J., Zhou J., Xiong W., Hedström P., Thuvander M., Selleby M. and Ågren J. (2012). 3D analysis of phase separation in ferritic stainless steels. Proceedings of the International Conference on 3D Materials Science, 2012, Pittsburg US.

Okada M., Thomas G., Homma M. & Kaneko H. (1978). Microstructure and magnetic properties of Fe-Cr-Co alloys. IEEE Trans. on Mag. **14**, 245-252.

Oppenheimer J.R. (1928). On the quantum theory of electronic impacts. Physical Review **32**, 361-376.

Park K.H., LaSalle J.C., Schwartz L.H. & Kato M. (1986). Mechanical properties of spinodally decomposed Fe-30wt% Cr alloys: yield strength and gaing embrittlement. Acta Metallurgica **34**, 1853-1865.

Porter D.A. & Easterling K.E. (1992). Phase transformation in metals and alloys, CRC Press.

Sassen J.M., Hetherington M.G., Godfrey T.J., Smith G.D.W., Pumphrey P.H. & Akhurst K.N. (1987). Kinetics of spinodal reaction in the ferrite phase of a duplex stainless steel. Properties of Stainless Steels in Elevated Temperature Service, Prager, M. (Eds.), pp. 65-78. New York: AMSE.

Stephenson L. T., Moody M. P., Liddicoat P. V. & Ringer, S. P. (2007). New techniques for the analysis of fine-scaled clustering phenomena within atom probe tomography (APT) data. Microscopy and Microanalysis **13**, 448-463.

Thermo-Calc. Database TCFE6, v. 6.2. Stockholm: Thermo-Calc Software AB; 2008.

Thuvander M., Zhou J., Odqvist J., Hertzman S. & Hedström P. (2012). Observations of copper clustering in a 25Cr-7Ni super duplex stainless steel during low-temperature aging under load. Philosophical Magazine Letters **92**, 336-343.

Vitek J. M. (1987). G-phase formation in aged type 308 stainless steel. Metallurgical and Materials Transactions A **18**, 154-156.

Warren P.J., Cerezo A. & Smith G.D.W. (1998). Observation of atomic planes in 3DAP analysis. Ultramicroscopy **73**, 261-266.

Williams R.O. & Paxton H.W. (1957). The nature of aging of binary iron-chromium alloys around 500 C. J. Iron Steel Inst. **185**, 358-374.

Woodilla J.E. & Averbach B.L. (1968). Modulated structures in Au-Ni alloys. Acta Metallurgica **16**, 255-263.

Xiong W., Hedström P., Selleby M., Odqvist J., Thuvander M. & Chen Q. (2011). An improved thermodynamic modeling of the Fe-Cr system down to zero kelvin coupled with key experiments. CALPHAD **35**, 355-366.

Zhou J., Odqvist J., Thuvander M., Hertzman S. & Hedström P. (2012). Concurrent phase separation and clustering in the ferrite phase during low temperature stress aging of duplex stainless steel weldments. Acta Materialia **60**, 5818-5827.

Zhou J., Odqvist J., Thuvander M. & Hedström P. (2013). Quantitative Evaluation of Spinodal Decomposition in Fe-Cr by Atom Probe Tomography and Radial Distribution Function Analysis. Microscopy and Microanalysis **19**, 665-675.